https://doi.org/10.5194/egusphere-2026-3561
Preprint. Discussion started: 30 June 2026

The diathermohaline stream function method for investigating the water mass transformation of the global ocean circulation (v2026.1)

Verena Jung[1], Aitor Aldama Campino[2], Joakim Kjellsson[2], and Kristofer Döös[1]

[1]Department of Meteorology, and Bolin Centre for Climate Research, Stockholm University, SE
[2]Rossby Center, Swedish Meteorological and Hydrological Institute, SE

Correspondence: Verena Jung (verena.jung@misu.su.se)

Abstract. In this work, we present a source code for computing the diathermohaline stream function, enabling the analysis of Water Mass Transformation from gridded ocean data within the thermohaline framework. This implementation extends previous versions by increasing the precision of the projection from geographical to thermohaline space. Using Helmholtz decomposition, the stream function represents the rotational component of thermohaline transformation vectors, while the divergent component defines the tendency potential. We show that the dominant global driver of the tendency potential is the net freshwater imbalance across the ocean boundary. Together, the tendency potential and the diathermohaline stream function provide a powerful yet underutilized method for comparing global Water Mass Transformation across ocean models. We demonstrate the utility of this framework using data from a coupled climate model, hindcast simulations, and an ocean reanalysis product, all based on the NEMO ocean model and spanning multiple spatial resolutions. The implementation is modular and user friendly, facilitating straightforward application to a wide range of oceanographic data sets. The code can also be applied to study water mass transformation using any tracer coordinates and to compute the meridional overturning stream function for generalised coordinates.

1 Introduction

The ocean plays an important role for the climate system by redistributing freshwater and heat around the Earth. Understanding the transformations of water mass properties is crucial when investigating the global ocean circulation (e.g Marshall and Speer, 2012) and its response to global warming. Water mass transformation (WMT) occurs to a large extent through air–sea interactions, which increase temperature and salinity gradients, and thus modify the buoyancy of water masses (e.g. Hieronymus et al., 2014). The main drivers are precipitation, evaporation, latent, sensible, and radiative heating and cooling, as well as river runoff, sea–ice melting, and brine rejection (Groeskamp et al., 2019). As heat fluxes increase the ocean's temperature particularly in tropical regions, the heat is further transported from low to high latitudes and thus, must also cross isotherms (Holmes et al., 2019). This diathermal heat transport balances the surface forcing through small-scale diffusive processes in the ocean's interior (Döös et al., 2012; Pemberton et al., 2015). Although these mixing processes are relatively weak, they act on a large volume and accordingly relax the gradients of temperature and salinity. These perspectives make WMT a fundamental concept for studying the ocean circulation. (Compare also Groeskamp et al., 2019, for a detailed review.)

https://doi.org/10.5194/egusphere-2026-3561
Preprint. Discussion started: 30 June 2026

The WMT framework was formalised by Walin in 1977 and 1982, when investigating ocean circulation in salinity and temperature, which led to a significant improvement of the knowledge gained previously by e.g. earlier box-model approaches. Several subsequent studies used this framework (e.g. Zika et al., 2015; Skliris et al., 2016, 2018) and extended the WMT approach to other ocean properties, such as density and buoyancy, broadening its relevance for diagnosing the mechanisms that drive the global circulation (e.g. Speer, 1997; Marshall et al., 1999; Nurser et al., 1999; Isachsen et al., 2007; Iudicone et al., 2008; Evans et al., 2017). A package for WMT diagnostics in ocean models was recently developed by Drake et al. (2025). Another major advance has been the use of stream functions in tracer space to provide compact representations of the circulation and the WMT. Döös and Webb (1994) demonstrated that representing the overturning circulation in latitude–density stream function removes the Deacon cell, a pronounced feature in latitude–depth coordinates, clarifying the role of isopycnal pathways and highlights the limitations of zonally integrated latitude–depth representations. Defining stream function in depth–density coordinates reveals whether the cell is driven thermally or mechanically (Nycander et al., 2007). These developments show the power of stream function diagnostics for revealing how water masses circulate and transform.

Building on those developments, Döös et al. (2012) and Zika et al. (2012) independently introduced the thermohaline stream function, representing only the advective modification of water mass temperature and salinity. Groeskamp et al. (2014) extended this concept to the diathermohaline stream function by incorporating non-advective displacements of isotherms and isohalines associated with diffusive processes and surface forcing. Applying analogous ideas to the atmosphere yields the hydrothermal stream function, which can be used to analyse atmospheric heat transport in latent heat and dry static energy, and its changes under climate forcing (Kjellsson et al., 2014; Kjellsson, 2015). Linking the oceanic diathermohaline and atmospheric hydrothermal stream functions shows that they are connected through exchanges of heat and freshwater across the sea surface (Döös et al., 2017). This demonstrates how tracer–space stream functions offer a concise and physically consistent framework for analysing these transformations.

Due to this condensed representation of ocean dynamics and its WMT, the diathermohaline stream function is a powerful diagnostic for comparing gridded ocean data (Groeskamp et al., 2014). Despite these advantages, the practical application of the diathermohaline stream function remains challenging. For its computation, ocean fields must be fully resolved in both space and time but observations of dynamical quantities rarely meet this requirement (Groeskamp et al., 2019). This makes ocean models particularly well suited for applications of the diathermohaline stream function, including model intercomparison projects. Nevertheless, it remains seldom used in such studies. To address these limitations, we present a modular Fortran code for computing the diathermohaline stream function, extending previous implementations used by Döös et al. (2012); Kjellsson et al. (2014); Ballarotta et al. (2014); Döös et al. (2017), through a more accurate projection of volume transports into thermohaline space. The code is designed to be easily adapted to other data sets. We demonstrate its utility by analysing present day (PD) data of a coupled climate model, ocean hindcast simulations of different horizontal resolutions and an ocean reanalysis product, all based on NEMO. Furthermore, we analyse a pre-industrial (PI) simulation and several climate scenarios of the coupled climate model. This illustrates how the diathermohaline stream function can contribute to comparison projects of gridded ocean data. The data sets provide differing sets of available model variables, and we assess the sensitivity of the

https://doi.org/10.5194/egusphere-2026-3561
Preprint. Discussion started: 30 June 2026

resulting diathermohaline stream functions to these differences. As validation data set, we use a ten year pre-industrial (PI) simulation from the Earth System Model EC-Earth3-Veg.

The paper is organised as follows. Sect. 2 presents the mathematical formulation and numerical implementation of the diathermohaline stream function. It is based on the Helmholtz decomposition, ensuring that the stream function is divergence free and contains no sinks and sources. We give a review of the studies that discuss the WMT shown by the diathermohaline stream function. The non-rotative part is represented by the tendency potential that we analyse as a result of the freshwater fluxes at the sea surface. Sect. 3 describes the data sets used, and Sect. 4 quantifies the sensitivity of the stream function to different model output variables. Sect. 5 compares the diathermohaline stream function across the NEMO configurations, and Sect. 6 discusses these results in relation to the water-volume distributions of the ocean basins in the given data sets. Sect. 7 concludes and gives final remarks. In the Appendix, we provide a sensitivity study of the stream function and the tendency potential on the thermohaline space resolution.

2 Method

2.1 Mathematical formulation

The definition of the diathermohaline stream function follows Döös et al. (2017), whereby the total tendencies of salinity and potential temperature are the sum of the advection by ocean currents and the time dependent, non-advective, displacements of the isosurfaces:

$$\dot{S}'(x,y,z,t) = \frac{\mathrm{D}S}{\mathrm{D}t} = \frac{\partial S}{\partial t} + \boldsymbol{u}\cdot\nabla S \quad \text{and} \tag{1a}$$

$$\dot{\theta}'(x,y,z,t) = \frac{\mathrm{D}\theta}{\mathrm{D}t} = \frac{\partial \theta}{\partial t} + \boldsymbol{u}\cdot\nabla\theta, \tag{1b}$$

with $\boldsymbol{u} = (u,v,w)$ the three-dimensional velocity vector. The tendencies have the units $\dot{\mathrm{S}}'\left(\mathrm{psu\,s^{-1}}\right)$ and $\dot{\theta}'\left(^{\circ}\mathrm{C\,s^{-1}}\right)$ and are defined in physical space, indicated by primes. The tendencies are projected onto thermohaline space by

$$\dot{S}(S,\theta) = \frac{1}{t_1-t_0}\int_{t_0}^{t_1}\int_{\Omega}\delta\left[S-S'(x,y,z,t)\right]\delta\left[\theta-\theta'(x,y,z,t)\right]\dot{S}'\,\mathrm{d}V\,\mathrm{d}t \quad \text{and} \tag{2a}$$

$$\dot{\theta}(S,\theta) = \frac{1}{t_1-t_0}\int_{t_0}^{t_1}\int_{\Omega}\delta\left[S-S'(x,y,z,t)\right]\delta\left[\theta-\theta'(x,y,z,t)\right]\dot{\theta}'\,\mathrm{d}V\,\mathrm{d}t, \tag{2b}$$

with an integration over the whole ocean volume Ω and a time average for the period from t_0 to t_1. The Dirac delta function is defined as $\int_{x-\epsilon}^{x+\epsilon}\delta[x]\,\mathrm{d}x = 1$ with $\epsilon > 0$ and $\delta[x] = 0$ for $x \neq 0$ and has the inverse unit of its argument. Thus, the projected tendencies have the units of $\dot{\mathrm{S}}\left(\mathrm{m^3\,s^{-1}\,{}^{\circ}C^{-1}}\right)$ and $\dot{\theta}\left(\mathrm{m^3 s^{-1}\,psu^{-1}}\right)$.

Defining stream functions is possible for divergence-free vector fields. The oceans' diahaline and diathermal tendencies are not purely rotational but incorporate a divergent component, arising from trends in salinity and potential temperature as well as net fluxes through the sea surface. Moreover, the averaging periods do not fully represent the ocean's natural variability, and

https://doi.org/10.5194/egusphere-2026-3561
Preprint. Discussion started: 30 June 2026

numerical model truncations and drift also contribute to the non-rotational component (Döös et al., 2017). Therefore the vector field $\left(\dot{S},\dot{\theta}\right)$ is separated into its rotational and divergent components by Helmholtz decomposition (Li et al., 2006; Watterson, 2001; Shukla and Saha, 1974). Using the non-dimensional nabla operator $\nabla_{S,\theta} = \left(\Delta S \frac{\partial}{\partial S}, \Delta\theta \frac{\partial}{\partial \theta}\right)$, the stream function ψ and the tendency potential χ are defined by the rational and the divergent part of the tendencies respectively:

$$\nabla^2_{S,\theta}\psi = (\Delta S)^2 \frac{\partial \dot{\theta}}{\partial S} - (\Delta\theta)^2 \frac{\partial \dot{S}}{\partial \theta} \quad \text{and} \tag{3a}$$

$$\nabla^2_{S,\theta}\chi = \Delta S \Delta\theta \left(\frac{\partial \dot{S}}{\partial S} + \frac{\partial \dot{\theta}}{\partial \theta}\right). \tag{3b}$$

The solutions of the Poisson equations Eq. (3) are the stream function ψ and the tendency potential χ. It is worth noting that the stream function shows the rotational part of the WMT resulting from, such as air–sea interaction and mixing processes, that act such that the global water volume reaches the same state in thermohaline coordinates within the considered time period. The tendency potential represents the WMT that is irrotational. It contains for example the sinks and sources of mass due to net evaporation and precipitation or internal variability in a global perspective represented in the thermohaline space. Consequently, the tendency potential is generally non-zero, even when the ocean was in a steady state, reflecting sources and sinks of mass in thermohaline space.

2.2 Numerical implementation

The implementation of the diathermohaline stream function is a further development of the ones by Döös et al. (2012); Kjellsson et al. (2014); Ballarotta et al. (2014); Döös et al. (2017). Its computation requires total tendencies (Eqs. (1)) that consist of the non-advective displacement of isosurfaces and the advective terms. For the projection of the advective terms from physical to thermohaline coordinates (Eqs. (2)), we use the zonal, meridional and vertical volume transports $\dot{U},\dot{V},\dot{W}$ $\left(\mathrm{m^3\,s^{-1}}\right)$. The horizontal volume transports are either taken from the model output files or computed from the model velocity fields with the model layer thicknesses. The volume transports in the vertical direction $\dot{W}$ are computed using the continuity equation. Figure 1 visualises the projection of the zonal volume transport $\dot{U}\,(x,y,z)$ onto thermohaline space for $\dot{S}\,(S,\theta)$ in the upper row and $\dot{\theta}\,(S,\theta)$ in the bottom row. The meridional and vertical indices j,k are removed from the graphics for better readability. During the computation of $\dot{S}\,(S,\theta)$, the volume transport $\dot{U}_{i,j,k}$ is added to all isohalines (m, $m+1$ and $m+2$) that are crossed. The linear slope $\Delta S/\Delta\theta$ between the two grid cells cell$_i$ and cell$_{i+1}$ in thermohaline coordinates is used to find the corresponding temperature index. Thus, $\dot{U}_{i,j,k}$ is added to the salinity tendencies $\dot{S}_{m,l}$, $\dot{S}_{m+1,l-1}$ and $\dot{S}_{m+2,l-2}$. This way of determining the corresponding temperature index is improved in precision compared to the previous versions, where the temperature index has been kept constant for all crossed isohalines.

The computation of the temperature tendency is done in a similar manner. In Fig. 1, the transport crosses the isotherm l and $l-1$. By applying a linear slope in thermohaline coordinates, the corresponding salinity indices are determined as $\dot{\theta}_{m,l}$ and $\dot{\theta}_{m+1,l-1}$. It is worth noticing, that the implementation evaluates one grid cell after another and considers the transports through all six adjacent cells when evaluating a single cell. This has the consequence that transports through grid cell walls is

https://doi.org/10.5194/egusphere-2026-3561
Preprint. Discussion started: 30 June 2026

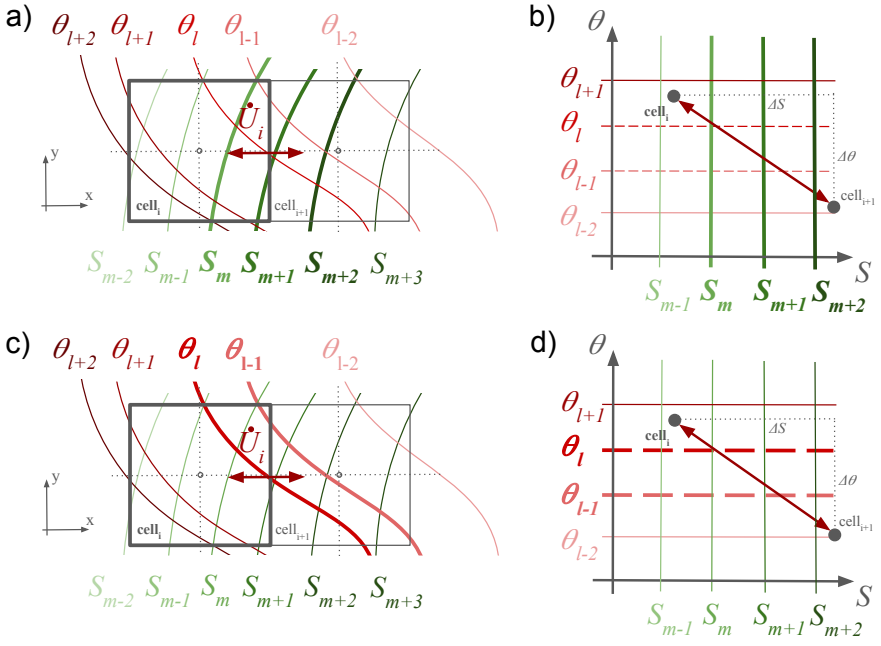

Figure 1. Visualisation of projecting the advective terms from geographical space (panels a) and c)) onto thermohaline space (panels b) and d)) for the example of zonal volume transport $\dot{U}_i$ between the grid cell$_i$ and cell$_{i+1}$. For simplicity, the meridional and vertical indices j and k are removed from the graphics. The upper (bottom) row shows the projection of the tendencies $\dot{S}$ ($\dot{\theta}$) whereby the volume transport $\dot{U}_i$ is added the isohalines (isotherms) that are crossed, indicated as bold lines. The corresponding index of the other tracer is determined by the slope ($\Delta\theta/\Delta S$) between the two grid cells in (S, θ) coordinates.

investigated twice. Therefore, the transports add only to the tendencies when the tracer gradient (∇S or $\nabla\theta$) along this transport is positive and the tracer value in the adjacent grid cell is larger. This ensures that each volume transport is added only once to the tendencies. In case of the example in Fig 1, the volume transport $\dot{U}_i$ is added to the tendency $\dot{S}\,(S,\theta)$ when evaluating grid cell$_i$, but it is added to the tendency $\dot{\theta}\,(S,\theta)$ when evaluating grid cell$_{i+1}$ since the value of potential temperature of the adjacent grid cell$_i$ is larger.

The projection of the partial derivatives $\partial S/\partial t$ and $\partial\theta/\partial t$ is done equivalent whereby each grid cell is compared in its properties to the previous time step. The time averaged volume of the grid cell is divided by the time step length and added or subtracted from the tendencies when the tracer value in the past time step is smaller or larger respectively. To remove trends from the data, the last time step is taken into account when $\partial S/\partial t$ and $\partial\theta/\partial t$ is computed for the first time step in Eqs. (1). Depending on the time period for which the stream function is computed, this might shift of the ocean volume in thermohaline space due to internal variability.

The Poisson equations (Eqs. (3)) are solved iteratively with the Successive Over Relaxation algorithm (Döös et al., 2022) with the tendencies' curl and the divergence as source terms for the diathermohaline stream function ψ and the tendency

https://doi.org/10.5194/egusphere-2026-3561
Preprint. Discussion started: 30 June 2026

potential χ. The applied boundary conditions are homogeneous Dirichlet Boundary Conditions ($\psi = \chi = 0$) on the convex hull of the tendencies in thermohaline space with allowing for a small number of $\epsilon = 0.1\mathrm{Sv}$ on the boundary. We show that the diathermohaline stream function is independent to the discretisation of the the thermohaline space, but the potential appears to be more sensitive while the general picture is robust here as well (shown in Appendix A). We speculate that this is caused by solving the discretised Eq. (3) using the definition of the non-dimensional nabla operator $\nabla^2_{S,\theta}$. For the computation of the stream function and the tendency potential of this study, we choose a discretisation of 500 bins for each tracer. With the ranges of salinity from 30–40 psu and θ from -3–37 $^\circ\mathrm{C}$, our thermohaline space has a resolution of 0.02 psu and 0.08 $^\circ\mathrm{C}$.

2.3 Review of the diathermohaline stream function

The diathermohaline stream function (Fig. 2) is characterised by three major cells. The red clockwise Conveyor Belt cell is to a large extent – though not exclusively – the global Thermohaline Circulation (Döös et al., 2012; Zika et al., 2012) since the subtropical gyres also contribute to it (Zika et al., 2013; Hieronymus et al., 2014). The blue anti-clockwise Tropical cell at warm temperatures represents mainly the WMT in the Indo-Pacific predominately resulting from the upwelling and warm pool and the wind driven tropical meridional cells (Döös et al., 2012). The blue anticlockwise Polar cell at colder temperatures is associated mainly with advection in the Arctic region and, even more importantly, with processes in the Southern Ocean with Antarctic Bottom Water formation. In addition to these large-scale cells, a weaker anticlockwise cell appears at temperatures 2–10 $^\circ\mathrm{C}$ and salinities 32.5–33.5 psu. Groeskamp et al. (2014) identified it as WMT by non-advective processes, specifically a combination of cryospheric processes and seasonal radiative heating in the North Pacific.

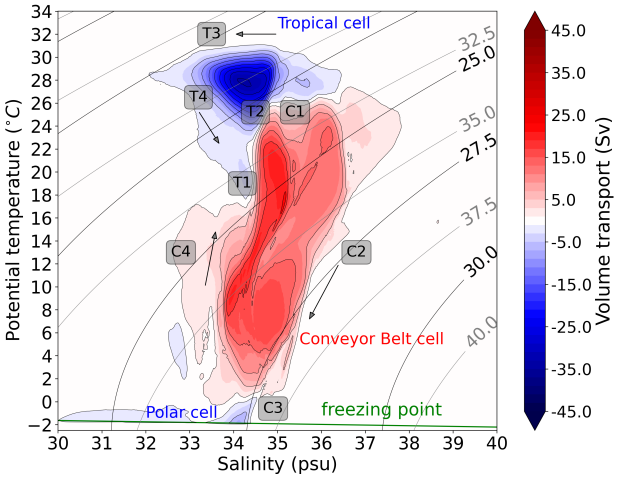

Figure 2. Schematics of the diathermohaline stream function. Red stream function cells rotate clockwise and blue cells anti-clockwise. The steps between the black contour lines are of 4 Sv starting with a magnitude of 1 Sv in both the clockwise and anticlockwise cells. The computation of σ isopycnals are done with the Thermodynamic Equation Of Seawater - 2010 (TEOS-10); σ_0 and σ_2 $\left(\mathrm{kg\,m^{-3}}\right)$ are labelled in back and grey respectively.

https://doi.org/10.5194/egusphere-2026-3561
Preprint. Discussion started: 30 June 2026

The Conveyor Belt cell spans a broad interval in the thermal direction and has been the focus of multiple studies to reconnect the sections (C1–C4 in Fig. 2) to geographical space and explain involved physical processes. First analyses refolded stream layers back into geographical coordinates (Döös et al., 2012; Zika et al., 2012) and identified the salinification branch (C1 in Fig. 2) at its warmest temperatures as warm and fresh waters flowing from the Pacific through the Indian Ocean into the Atlantic (Döös et al., 2012). The subsequent cooling and freshening (C2 in Fig. 2) divide into two branches. Both originate through surface fluxes, and further cooling and freshening along both branches arise from a combination of surface fluxes and isoneutral diffusion (Hieronymus et al., 2014). The fresher branch is primarily located in the Indo-Pacific, while the saltier branch contains Atlantic water masses flowing northward. Berglund et al. (2017) simulated Lagrangian trajectories initialised at 17 °S with properties of South Atlantic Central Water, AAIW, and deep water. These trajectories terminated at 58 °N, at which point most of the water masses had reached salinities between 34.5 and 35.5 psu and temperatures of 5–10 °C, characteristic of North Atlantic central water and NADW. Major parts of the cooling and freshening occur along the northern flank of the subtropical gyre, the North Atlantic drift and Gulf stream. In this region, water masses mix with those originating in the Labrador Sea and circulate within the subtropical gyre before flowing again northward. Berglund et al. (2017) also concluded that further cooling and freshening takes place further north of 58 °N where North Atlantic Deep Water is formed at around 35 $\mathrm{g\,kg^{-1}}$ and 5 °C (Zika et al., 2013), mainly due to air–sea interaction since the mixed layer is usually deep (Berglund et al., 2017).

In the Southern Ocean, the upwelling of deep water and formation of AAIW in the Southern Ocean (C3 in Fig. 2) are characterised by a net freshening and warming (Evans et al., 2018). In the annual mean, AAIW is destroyed by surface fluxes while dianeutral and isoneutral diffusion act to produce AAIW (Hieronymus et al., 2014). However, Evans et al. (2018) showed that the associated process exhibit a strong seasonality. During winter, AAIW is cooled by surface heat loss and salinified by brine rejection. This dense winter water close to the freezing point mixes isoneutral below the surface with the Antarctic deep water particularly in the Weddell gyre and Atlantic sector (Hieronymus et al., 2014; Evans et al., 2018). During summer, AAIW is formed, when the winter water is warmed by surface fluxes and freshened by sea ice melt (Evans et al., 2018). The effect of the seasonality was also documented by Berglund et al. (2021) who found with Lagrangian simulations that waters in the momentary mixed layer near the Antarcitc ice shelfs experience salinification that can be explained by brine rejection. In contrast, the maximum mixed layer, show a strong freshening, especially in the Weddell Sea, corresponding to the net freshening observed by Evans et al. (2014). Below the maximum mixed layer, salinity remains unchanged, highlighting the importance of seasonal air–ice–sea interaction.

The warming and salinification branch of the Conveyor Belt cell (C4 in Fig. 2) can be, to a large extent, explained by water masses flowing from the Southern Ocean equatorward. Berglund et al. (2021) initiated Lagrangian trajectories in the Drake Passage, and computed them from the 2 °C isotherm until they have reached the 25 °C isotherm. The Lagrangian stream function of the northward flowing trajectories corresponds to the Eulerian stream function with 78 % at the 10 °C and 15 °C isotherm. This indicates that these pathways represents a major component of the Conveyor Belt cell part. The trajectories follow the ACC, before they flow northward into the ocean basins in the east and turn westward in the subtropical gyres from where they exit and continue northward without recirculation in the gyres. The net heat gain in the ACC is governed by a

https://doi.org/10.5194/egusphere-2026-3561
Preprint. Discussion started: 30 June 2026

seasonality. Water cools within the momentary mixed layer during autumn and winter and warms in the maximum mixed layer mainly during spring and summer. Further warming occurs in the subtropical gyres and at the equator due to surface fluxes and mixing with other, warmer water masses. Salinification takes place in the southern parts of the subtropical gyres due to evaporation and in the eastern and northern parts of the subtropical gyres through mixing with other water masses below the maximum mixed layer depth.

This salinification due to mixing was also discussed by Zika et al. (2013), who analysed the Conveyor Belt cell as a combination of a deep, thermally indirect cell at colder temperatures and a warm, thermally direct surface cell. Both cells rotate clockwise in thermohaline coordinates and overlap in the thermohaline space at a potential temperature range of 12–15 °C. This overlap is also visible in Fig. 2. Although, these cells are not connected in temperature-depth or in depth–latitude coordinates, they form an interconnected circulation in thermohaline space because they involve the same water masses. Thus, they constitute the Conveyor Belt cell. The thermally direct surface cell corresponds to the subtropical gyres, while the deep cell represents the upper limb of the meridional overturning circulation. The salinity gain in the deep cell results primarily from mixing with the subtropical gyres.

The Tropical cell is determined by WMT in the Indo-Pacific (Döös et al., 2012) and can also be structured in four segments. Firstly, a minimum temperature where water masses subduct into the thermocline adiabatically, from where they flow eastward and equatorward, and upwell in the cold pool of the eastern Pacific (T1 in Fig 2). The second segment overlaps with the salinification branch of the Conveyor Belt cell (T2 in Fig. 2). It is explainable by waters flowing westward while increasing in temperature and salinity due to surface fluxes that are opposed by isoneutral and dianeutral diffusion (Hieronymus et al., 2014). The overlap implies that the Tropical cell and the Conveyor Belt cell partly cancel each other, and span, in fact, over a larger region in the thermohaline space. As the water continues to flow westward (segment T3), the salinity decreases at nearly constant temperatures since the warming by surface fluxes is opposed by dianeutral diffusion (Hieronymus et al., 2014). This is followed by a cooling segment (T4), where salinity increases mainly due to dianeutral diffusion (Hieronymus et al., 2014).

The Polar cell is primarily a result from WMT in the Southern Ocean. Stewart (2021) conducted a regional analysis of a diathermohaline stream function in the Weddell Sea to examine WMT beneath ice shelves and the formation of Weddell Sea Deep water, which contributes 40–50 % to the production of the Antarctic Bottom Water. The resulting diathermohaline stream function appears in the structure of the global Polar cell with a magnitude of approximately -8 Sv, similar to the magnitude of the Polar cell in Fig. 2, though extending to higher salinities. Stewart (2021) also found that the mean flow and eddies, defined as all processes on sub-monthly time scales, contribute nearly equally to the WMT in their regional diathermohaline stream function.

2.4 Tendency potential

Döös et al. (2017) applied a Helmholtz decomposition for the computation of the diathermohaline stream function. They discuss the tendency potential as a consequence of trends in salinity and temperature due to forcing, variability, model errors, and imperfect ocean mass conservation. Here, we investigate the contribution of the net sinks and sources from freshwater fluxes across the oceans' boundaries to the tendency potential. We use a historical simulation of 50 years with the EC-Earth3-

https://doi.org/10.5194/egusphere-2026-3561
Preprint. Discussion started: 30 June 2026

Veg CMIP6 simulation (1851–1900) to limit the impact of climate change and to take inter decadal variability better into account. We project the volume fluxes across the oceans' boundaries (evaporation, precipitation, river run off, ice melting and freezing) into thermohaline space (panel a) in Figure 3) and solve the Poisson equation with this quantity as source term (panel b) in Figure 3). Panel c) shows the tendency potential χ for which Eq. (3) is solved with the divergence of the tendencies as source term.

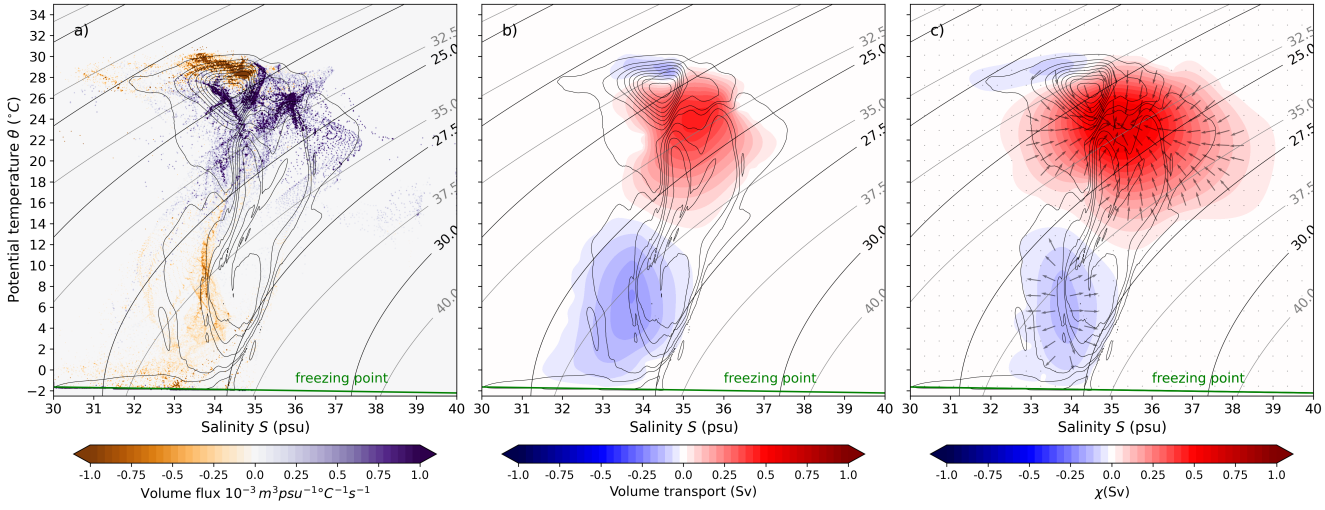

Figure 3. Volume fluxes into the ocean in thermohaline space (panel a)), its solution of the Poisson equation (panel b)), and the tendency potential χ (panel c)) for a CMIP6 EC-Earth3-Veg simulation (1851–1900). The black arrows in panel c) indicate the divergent parts of the diathermohaline tendencies. The superimposed grey contour lines is the diathermohaline stream function in 4 Sv intervals starting with a magnitude of 1 Sv for all cells. The isopycnals σ_0 and σ_2 $\left(\mathrm{kg\,m^{-3}}\right)$ are labelled in back and grey respectively.

The solutions of the two Poisson equations are in good agreement in magnitude and shape. Specifically, considering that the quantity in the middle panel is computed on two-dimensional fields and the one in the right panel on three-dimensional ocean data. Furthermore, both incorporate truncation errors caused by the projection from geographical space to thermohaline space. Thus, we argue that most of the tendency potential of the diathermohaline fluxes can be explained through the net fluxes of freshwater that act as source term driving the potential. Contributions from mixing and model drift are minor. We further include the diathermohaline stream function and superimpose it to Fig. 3 as grey contour lines. This combined representation is in agreement with the discussion of Hieronymus et al. (2014) and Döös et al. (2017). The freshening branch in the Tropical cell of the diathermohaline stream function aligns with net precipitation in the warm water pool. The warming and salinification sections of the Tropical and Conveyor Belt cell aligns with net evaporation in the subtropics and partly the tropics. The freshening of the Polar cell and the Conveyor belt cell at cold temperatures is aligned with net precipitation in the polar and subpolar regions.

https://doi.org/10.5194/egusphere-2026-3561
Preprint. Discussion started: 30 June 2026

3 Data

3.1 Data description

The diathermohaline stream function is computed for multiple data sets whereby all of them are based on the ocean model NEMO (Madec et al., 2017). It uses the Boussinesq approximation with a reference density (ρ_0) and only the hydrostatic balance equation uses in situ density. The model conserves volume and the mass is a product of volume and ρ_0 (Bacon et al., 2015). They are defined on the ORCA tripolar grids of 1° and 1/12° horizontal resolution which correspond on the equator to approximately 110 km and 9.3 km respectively. The grids are defined with a global orthogonal curvilinear ocean mesh with two North Poles over land to avoid singularities within the computational domain (Madec and Imbard, 1996). The ORCA grids are of a C-grid structure with the scalar values defined in the centre of the grid cells and the transports and velocities defined on the grid cell interfaces. All data sets are evaluated using monthly averaged data for the ten year time period 2003–2012 for present day climate (PD).

The EC-Earth3-Veg model is a coupled earth system model where the ocean model is NEMO3.6 of 1° horizontal resolution and 75 vertical layers (Döscher et al., 2022). It is coupled to the Louvain-la-Neuve sea ice model LIM3, the atmosphere model IFS 36r4, land surface component HTESSEL and the vegetation model LPJ-GUESS . Additional to the PD simulation, we investigate pre-industrial (PI) for the years 1851–1860 and the climate scenarios ssp1-2.6, ssp3-7.0, ssp5-8.5 for the years 2091–2100 (SSP) (O'Neill et al., 2016). For all these CMIP6 simulation data we use the member r2i1p1f1 that is integrated from the 500 years piControl simulation after model spin-up.

The ocean-only (OGCM) simulations of 1° and 1/12° horizontal resolution, in the following called OGCM-1° and OGCM-1/12°, are global ocean simulations with the NEMO version 3.6 and the coupled sea ice model LIM2 (Wilson et al., 2021). Both model resolutions have 75 vertical model layers. The atmospheric forcing is the Drakkar forcing set (DFS) 5.2 (Dussin et al., 2016). NEMO in the 1/12° resolution contains no parametrisations for the lateral mixing due to eddies since it is eddy-resolving in most parts of the ocean (Bacon et al., 2015). Thus, the OGCM-1/12° data, contain the subgrid-scale diffusive parametrisations as part of the advective velocities (Wilson et al., 2021).

The GLORYS12 data set is a ocean reanalysis product with 1/12° horizontal resolution and 50 vertical layers. It is based on the NEMO model version 3.1 the is coupled to the sea ice model LIM2 whereby its sea surface is forced by the ECMWF ERA-Interim reanalysis data product (Jean-Michel et al., 2021). GLORYS12 is the only data set containing data assimilation (DA) of SST, sea level anomaly, in situ temperature and salinity profiles, and sea ice concentration. The data set contains the river run off from the climatological run off by (Dai et al., 2009) and the freshwater fluxes from icebergs for Greenland and Antarctica.

All NEMO data sets used here (OGCM simulations, EC-Earth3-Veg and GLORYS12) use a turbulent kinetic energy (TKE) closure model for vertical eddy viscosity and diffusivity. The OGCM-1/12° and GLORYS12 data are "eddy-rich" and thus contain the mesoscale eddy transports as part of the advective velocities (Wilson et al., 2021). Both ORCA1 configurations (EC-Earth3-Veg and OGCM-1°) use the Gent-McWilliams parametrisation (Gent and Mcwilliams, 1990) of mesoscale eddy-

https://doi.org/10.5194/egusphere-2026-3561
Preprint. Discussion started: 30 June 2026

induced turbulence for the horizontal tracer diffusion (Treguier et al., 1997). They are included in the volume transports of the EC-Earth3-Veg and are not used when calculating the OGCM-1° transports.

Zika et al. (2012) did investigations on the effect of the time mean eddy induced velocities with the University of Victoria Climate Model with the ocean component Geophysical Fluid Dynamics Laboratory (GFDL) Modular Ocean Model version 2.2 (MOM2) of 1.8° latitude and 3.6° longitude resolution. We repeat the investigations by Zika et al. (2012) for the NEMO3.6 model of 1° resolution using EC-Earth3-Veg simulation data for a pre-industrial time period of 10 years in Sect. 4 to determine the effect of including the parameterised eddy transports or not.

3.2 Meridional overturning stream function

Figure 4 shows the zonally integrated global meridional overturning stream function in latitude–depth coordinates for all data sets (upper row) and as a function of of σ_0, σ_2, θ and S for the OGCM-1/12° as representative data set (lower row). Comparing the different data sets, the bottom overturning cell (blue) and the Deacon cell of the EC-Earth3-Veg simulation has a weaker magnitude compared to the other data sets. The OGCM-1° and OGCM-1/12° show a deeper surface cell in the Southern Hemisphere compared to EC-Earth3-Veg and GLORYS12. The low-resolution models (EC-Earth3-Veg and OGCM-1°) both exhibit weaker and shallower upper-ocean cells compared to the eddy-rich models (OGCM-1/12° and GLORYS12), likely due to them having a stronger AMOC which is a common feature in NEMO simulations (Roberts et al., 2020; Sieker et al., 2026). The overturning cells are almost distinct hemispherical cells in the GLORYS12 data.

The overturning stream functions in the bottom row of Fig. 4 are computed by integrating over the axis of $\sigma_0, \sigma_2, \theta$ and S respectively. Accordingly, open stream lines appear due to sinks and sources throughout the integration domain that in fact occur at the sea surface due to evaporation and precipitation. These are not visible in depth coordinates since the the sea surface is the upper boundary for the integration. In tracer coordinates, however, the upper integration boundary is not necessarily on the sea surface. One possibility would be to solve the overturning stream functions as well with Helmholtz decomposition to separate first the sinks and source terms with a divergent part.

3.3 Area distribution function and comparison to satellite data

Since a significant part of the WMT takes place at the sea surface, an area distribution function $a\,(S,\theta)$ is defined and computed for all data sets following Hieronymus et al. (2014):

$$a(S,\theta) = \frac{1}{t_1 - t_0} \int_{t_0}^{t_1} \frac{\partial^2 A}{\partial S \partial \theta} dt \tag{4}$$

where $A = A\,(S,\theta,t)$ is the volume with a salinity less than S and a temperature less then θ.

Figure 5 shows the area distributions for all data set and compares it to the area distribution of the satellite product SMOS-SMAP (SSS SMOS/SMAP L4 OI - LOPS-v2023). This satellite data set is based on optimal interpolation methods of the ESA Soil Moisture and Ocean Salinity (SMOS) satellite and of the combined NASA Soil Moisture Active Passive (SMAP) satellite data from 2015. It reduces the large-scale and time-varying bias from the subtropical to subpolar latitudes compared to other

https://doi.org/10.5194/egusphere-2026-3561
Preprint. Discussion started: 30 June 2026

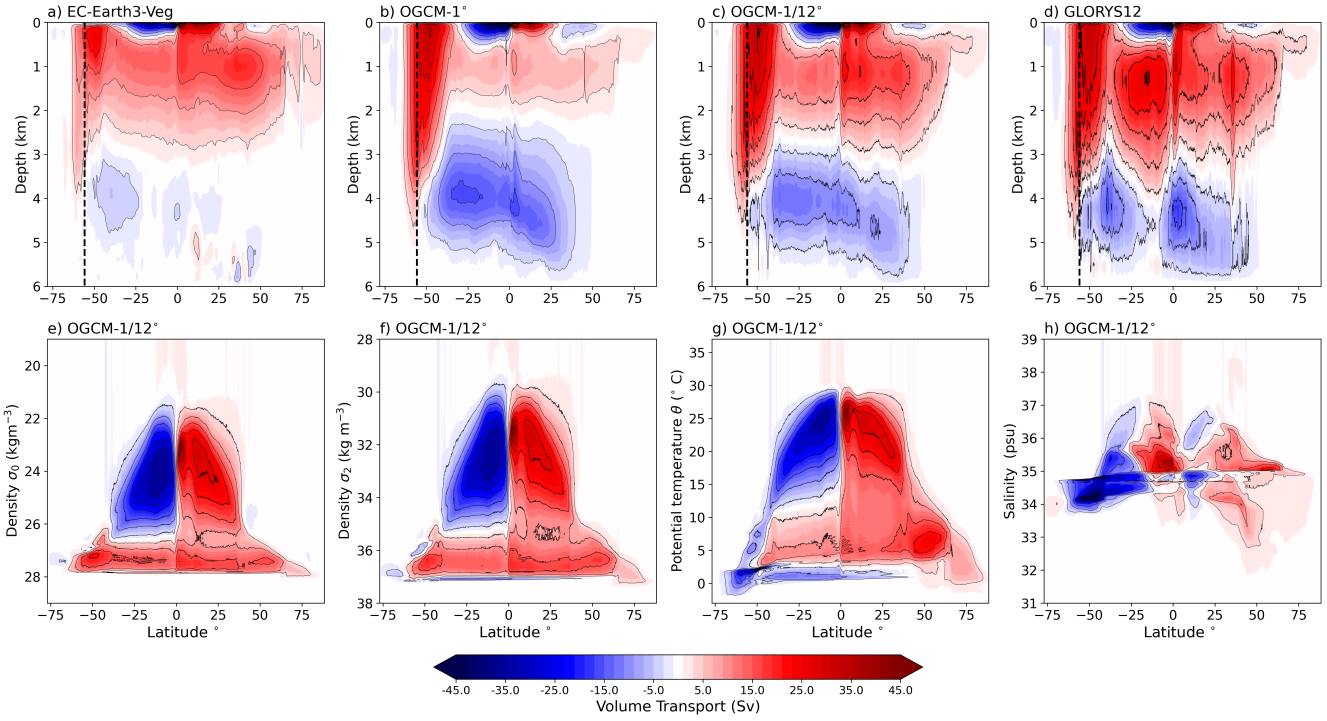

Figure 4. Meridional overturning stream functions as function of depth for the four different data sets described in Tab 1 (upper row) and as function of $\sigma_0, \sigma_2, \theta$ and S for the OGCM-1/12° as representative data set (bottom row). Red stream function cells rotate clockwise and blue cells anti-clockwise. The steps between the black contour lines are of 6 Sv starting with a magnitude of 3 Sv in both the clockwise and anticlockwise cells. The dashed vertical lines in the upper row indicate the used Southern Ocean boundary used in Sect. 6.

satellite SSS products by correcting biases under the use of in situ observations mainly from Argo data. Kolodziejczyk et al. (2021) gives a detailed description about the satellite data product SMOS-SMAP.

The overall structure of the distribution in thermohaline space is comparable between the satellite data and the model data. Specifically, the volume distributions of the high resolution simulation data the satellite data show a high degree of agreement with the greatest deviation located close to the freezing line. Kolodziejczyk et al. (2021) discusses larger errors of the SSS retrievals in the satellite data product in polar regions due to e.g. the SMOS and SMAP data resolution as well as limited Argo data. It is noticeable that the coarse 1° resolution model data are covering less the extreme salinity values compared to the fine resolution model data and the satellite data. The EC-Earth3-Veg data differ from the OGCM-1° data in terms of smoothness where some parts in temperature - salinity space do not show any surface water. The EC-Earth3-Veg simulation is using a free simulation with a coupling to an atmospheric model while the OGCM is forced by atmospheric reanalysis data and is therefore expected to represent the surface distribution more realistic. EC-Earth3-Veg has less water volume in the low temperature

https://doi.org/10.5194/egusphere-2026-3561
Preprint. Discussion started: 30 June 2026

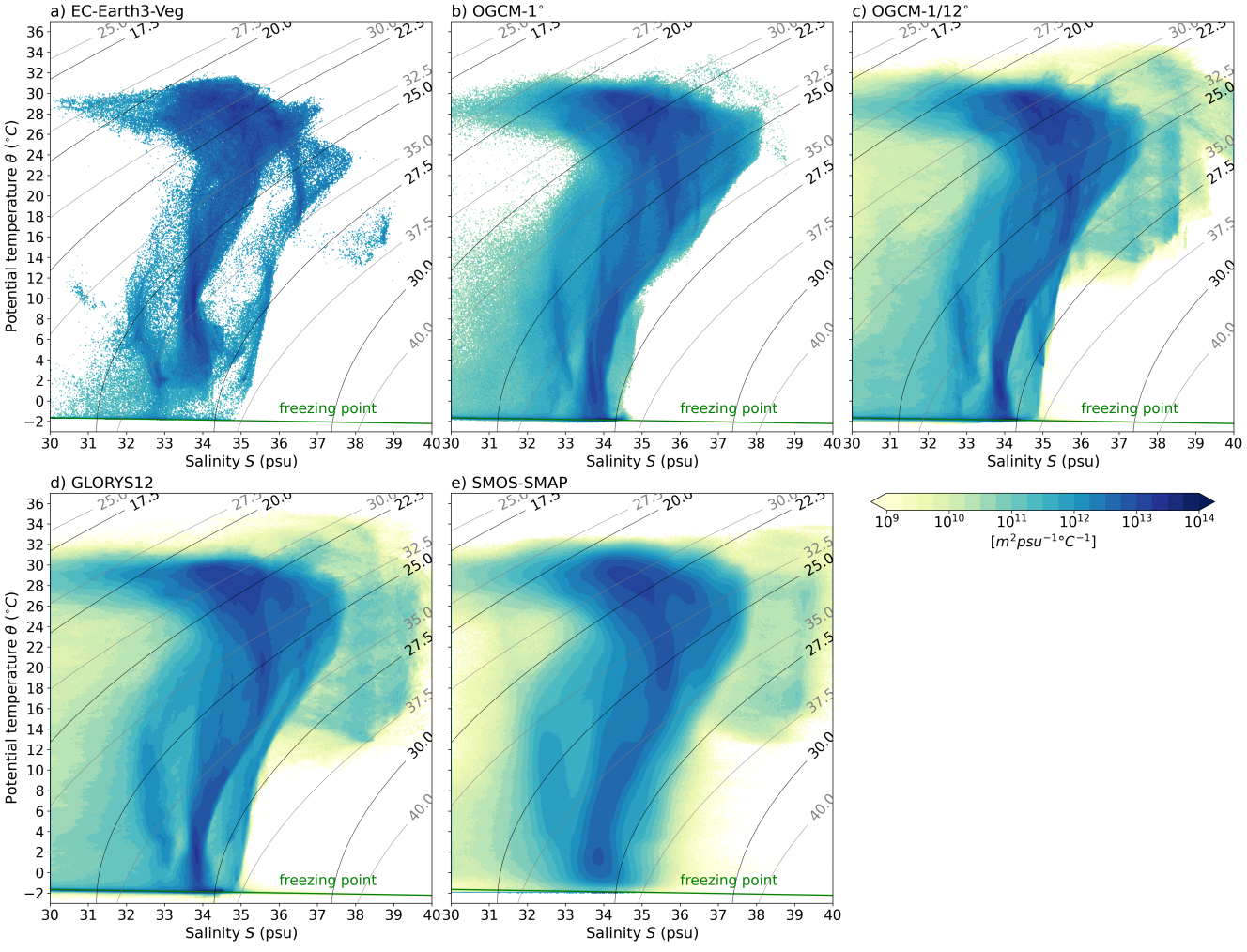

Figure 5. Area distribution functions $a(S, \theta)$ of global ocean surface water in thermohaline space of the four investigated data sets described in Tab. 1 (panels a)-d)) and the satellite product SMOS-SMAP (panel e)). The isopycnals σ_0 and σ_2 $\left(\mathrm{kg\,m^{-3}}\right)$ are labelled in back and grey respectively.

range close to the freezing line as well. We explain this by the known warm-bias of the model in the Southern Ocean and the under-representation of sea ice cover (Döscher et al., 2022).

3.4 Model output variables

Ideally, the advective part of the diathermohaline stream function is computed using the time averaged volume or mass transports computed online with the Eulerian mean velocities and the parametrised eddy-induced velocities. Otherwise, the volume transports need to be computed on the time averaged model output variables. Table 1 summaries the model output variables

https://doi.org/10.5194/egusphere-2026-3561
Preprint. Discussion started: 30 June 2026

Table 1. Overview of data sets, their spatial and temporal resolution, the applied ocean forcing, if data assimilation (DA) is incorporated and the provided model output variables that are used for the computation of the diathermohaline stream function. For this computation, volume or mass transports $\dot{m}$ and the time dependency, three-dimensional cell thicknesses are needed $dz_t\,(x,y,z,t)$. If these variables are not provided, the listed alternative model output variables are used and the computational steps (1)–(4) are applied.

Data set	Spatial resolution	Temporal resolution	Ocean forcing	DA	Output for $\dot{V}$	Output for dz
EC-Earth3-Veg	1°, 75 mod. lev.	1 month	Coupled	non	$\dot{m}^{(1)}$	$dz_t\,(x,y,z,t)$
OGCM-1°	1°, 75 mod. lev.	1 month	Drakkar 5.2	non	$\boldsymbol{v}^{(2)}$	$dz_t\,(x,y,z)$, $\eta\,(x,y,t)^{(3),(4)}$
OGCM-1/12°	1/12°, 75 mod. lev.	1 month	Drakkar 5.2	non	$\boldsymbol{v}^{(2)}$	$dz_t\,(x,y,z,t)^{(4)}$
GLORYS12	1/12°, 50 mod. lev.	1 month	ERA5	yes	$\boldsymbol{v}^{(2)}$	$dz_t(x,y,z)$, $\eta\,(x,y,t)^{(3),(4)}$

Computational steps:
(1) Division by the mean density ρ_0,
(2) Multiplication with cell thicknesses at u- and v-points dz_u and dz_v of the C-grid,
(3) Computation of a scaling factor of the vertical water column from the sea surface elevation η, assuming that all layers stretch and shrink with the same factor.
(4) Interpolation of dz_u, dz_v.

in the investigated data sets and the necessary steps in the computation of the volume transports. The following Sect. 4 investigates the sensitivity of the stream function to those differences in a specifically created NEMO3.6 validation data set. The EC-Earth3-Veg data set is the only one containing mass transports as model output while all the other data sets provide information about the ocean dynamics as velocities. For these data, we compute the volume transport from the time mean velocities fields and the time mean cell thicknesses. The data sets OGCM-1/12° and EC-Earth3-Veg include time dependent, three-dimensional layer thicknesses but OGCM-1° and GLORYS12 provide only time dependent sea surface elevations and the time fixed ocean layer thicknesses. Therefore, we compute here the time varying ocean layer thicknesses from the sea surface elevation assuming that all layers in a column are stretched and shrunk with the same factor. We expect this assumption to have little impact on the resulting stream functions. Since the OGCM-1° data set contains only the Eulerian mean velocities but not the eddy induced velocities, we also evaluate this contribution for in the NEMO validation data set.

4 Sensitivity of the diathermohaline stream function to model output variables

The time averaged volume transport can be Reynold decomposed into the sum of a product of the mean terms and the mean of the product of the fluctuation terms (e.g. Zika et al., 2013) as shown with the example of the meridional transports by Eq. (5)

$$\overline{v\Delta z}^{t}\,\Delta x = \overline{v}^{t}\,\overline{\Delta z}^{t}\,\Delta x + \overline{v'\Delta z'}^{t}\,\Delta x, \tag{5}$$

where the time average is notated with an overbar.

We compute the diathermohaline stream function with the product of temporal means for three of the four data sets (Sect. 3.4) and miss out the fluctuation term of the Reynolds decomposition (Eq. (5)). We, therefore, analyse the contribution of the terms in the Reynolds decomposition to the diathermohaline stream function. Since the OGCM-1° data do not contain the

https://doi.org/10.5194/egusphere-2026-3561
Preprint. Discussion started: 30 June 2026

eddy-induced velocities, we are also investigating their contribution. For this, we create a validation data set which is a 11 years (1850–1860) pre-industrial simulation with the EC-Earth3-Veg model using the initial conditions (member r1) of a 500 year piControl experiment with 80 years time lag that was integrated from a spin-up simulation (Jung, 2026). The EC-Earth3-Veg model with the ocean component NEMO3.6 is the same model as described in Sect. 3.1. All date are stored as monthly means and to cover the same number of years we use only the years 1851–1860 to compute the diathermohaline stream function. Zika et al. (2012) conducted a similar investigation for MOM2 model data. They compared the stream functions that are computed with monthly mean velocities and with velocities averaged over the whole time period identifying the contribution from inter annual and seasonal variability contributing to their stream function. The Tropical and the Conveyor Belt cells showed the main difference with a maximum of 5 Sv at a potential temperature of about 15 °C and an absolute salinity of 35 $\mathrm{g\,kg^{-1}}$. They further showed that even if eddy-induced velocities are weak in most of the ocean they contribute not negligible to the diathermohaline stream function of the MOM2 model data. Figure 6 shows the meridional overturning stream function and the area distribution

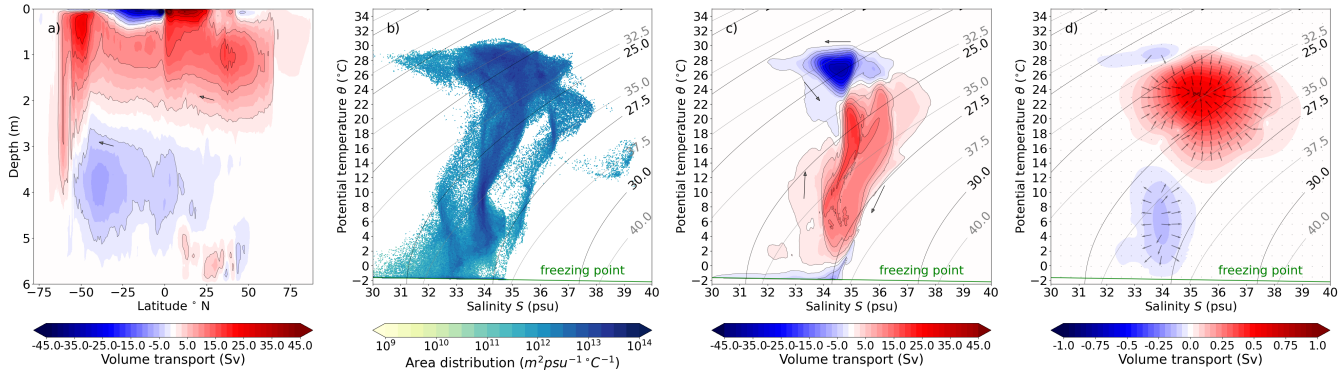

Figure 6. a) Meridional overturning stream function and b) area distribution function of the ten year PI (1851–1860) EC-Earth3-Veg validation data set. The diathermohaline stream function ψ (panel c)) and the tendency potential χ (panel d)) are computed with monthly mean volume transports. Red (blue) stream function cells indicate a clockwise (anticlockwise) rotation. Red convergence zones in the potential indicate net sinks and blue divergence zones indicate net sources.

function of the simulation data as well as the diathermohaline stream function and the tendency potential computed using the monthly averaged volume transports. Thus, it corresponds to the stream function computed with the volume transport of the left hand side (LHS) in Eq. (5). The stream function and the potential computed using the first term on the right hand side (RHS) is shown in the panel a) and b) of Fig. 7 respectively. Panel c) and d) in Fig. 7 show the stream function and the potential computed with velocities not containing the eddy induced part. The bottom row in Fig. 7 show the difference of the quantities shown in the top row with respect to the stream function computed with the volume transport (panel c) and d) in Fig. 6). The difference in the stream function computed with the time mean volume transport and the time mean velocities including eddy induced velocities is with a maximum absolute value of 2.8 Sv smaller compared to the difference of 5 Sv due to interannual and seasonal variabilities computed by (Zika et al., 2012).

https://doi.org/10.5194/egusphere-2026-3561
Preprint. Discussion started: 30 June 2026

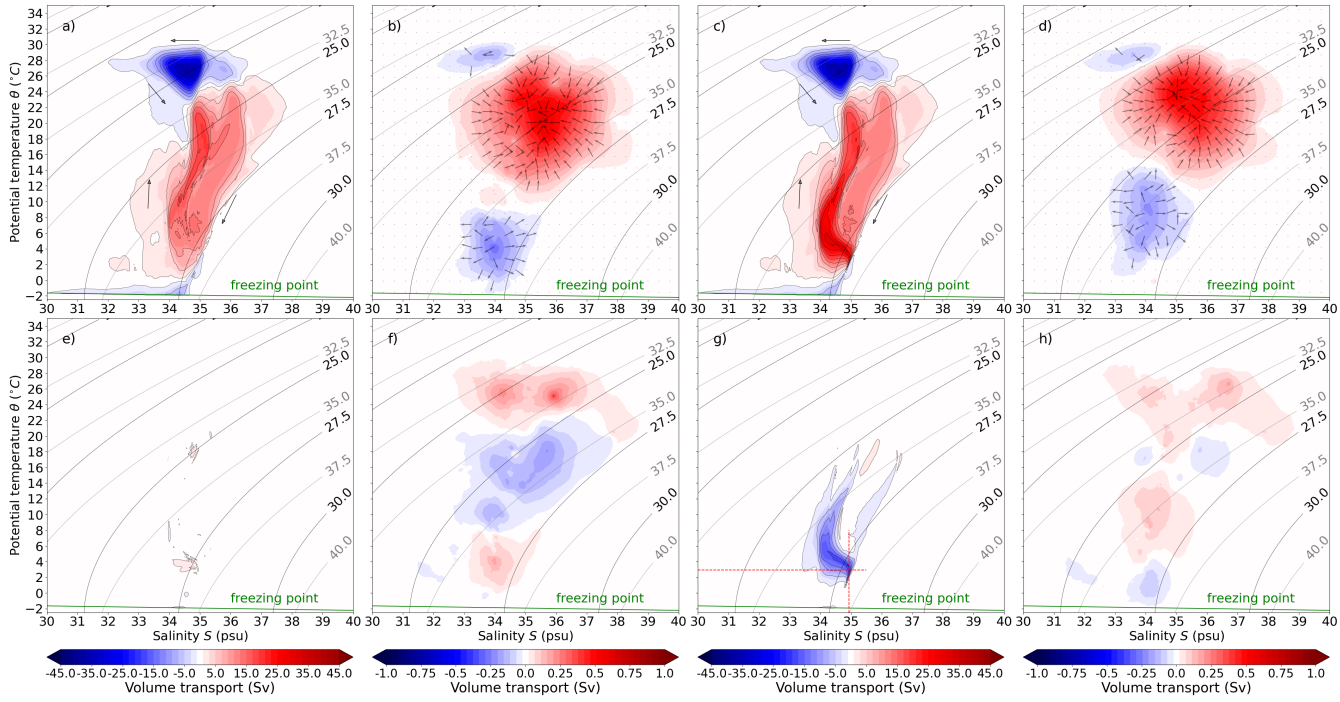

Figure 7. Stream functions Ψ and tendency potential χ of EC-Earth3-Veg validation data for the ten years PI simulation (1851–1860) computed with monthly model means using the time averaged velocities multiplied with time averaged area that is crossed by the flux. Red (blue) stream function cells indicate a clockwise (anticlockwise) rotation. Red convergence zones in the potential indicate net volume sinks and blue divergence zones indicate net volume sources. Black (grey) contour lines show the σ_0 (σ_2) isopycnals $\left(\mathrm{kg\,m^{-3}}\right)$. Panels a) and b) include both the Eulerian mean and eddy induced velocities while the panels c) and d) include only the Eulerian mean velocities. The bottom row (panel e) – h)) shows the difference with respect to ψ and χ computed with the volume transport (panel c) and d) in Fig. 6).

However, the contribution by the eddy induced velocities is larger with an absolute maximum of 21.6 Sv. This is at salinities of 34.9 psu and a potential temperature of 2.9 °C indicated by the red dotted lines in panel g) in Fig. 7. The reference stream function computed with volume transports has a magnitude of 4.5 Sv while the stream function without eddy induced velocities has strength of 26.1 Sv. Thus, the eddy induced velocities counteract the water mass transformation from the Eulerian mean velocities in the temperature range of 2–15 °C and a salinity of 33.5–35 psu. The shape in thermohaline space is very similar to the one found by (Zika et al., 2012) but they identified smaller values of 5–10 Sv by eddy induced velocities and connect that mainly to the Southern Ocean where isopycnals are steep.

https://doi.org/10.5194/egusphere-2026-3561
Preprint. Discussion started: 30 June 2026

5 Data comparison with the diathermohaline stream function

We use the diathermohaline stream function to identify differences in four data sets in present day model data and further present the diathermohaline stream function of a PI EC-Earth3-Veg simulation and three climate scenarios (ssp1-2.6, ssp3-7.0, ssp5-8.5). Integrating the stream function gives information about the transport of heat and freshwater.

5.1 Diathermohaline stream function in present day model data

The upper row of Fig. 8 shows the diathermohaline stream function of the four different data sets, summarised in Tab. 1, for the PD simulations. They are comparable in their general appearance, as all of them show the three main cells Tropical, Conveyor Belt and Polar cells. The weak blue NP radiative cell at 5 °C and 32–33 psu and the Cryosphere cell along the freezing line are visible for all data sets with an exception for the OGCM-1° data. The Polar cell is most pronounced in the EC-Earth3-Veg simulation and almost not visible in the OGCM of high resolution.

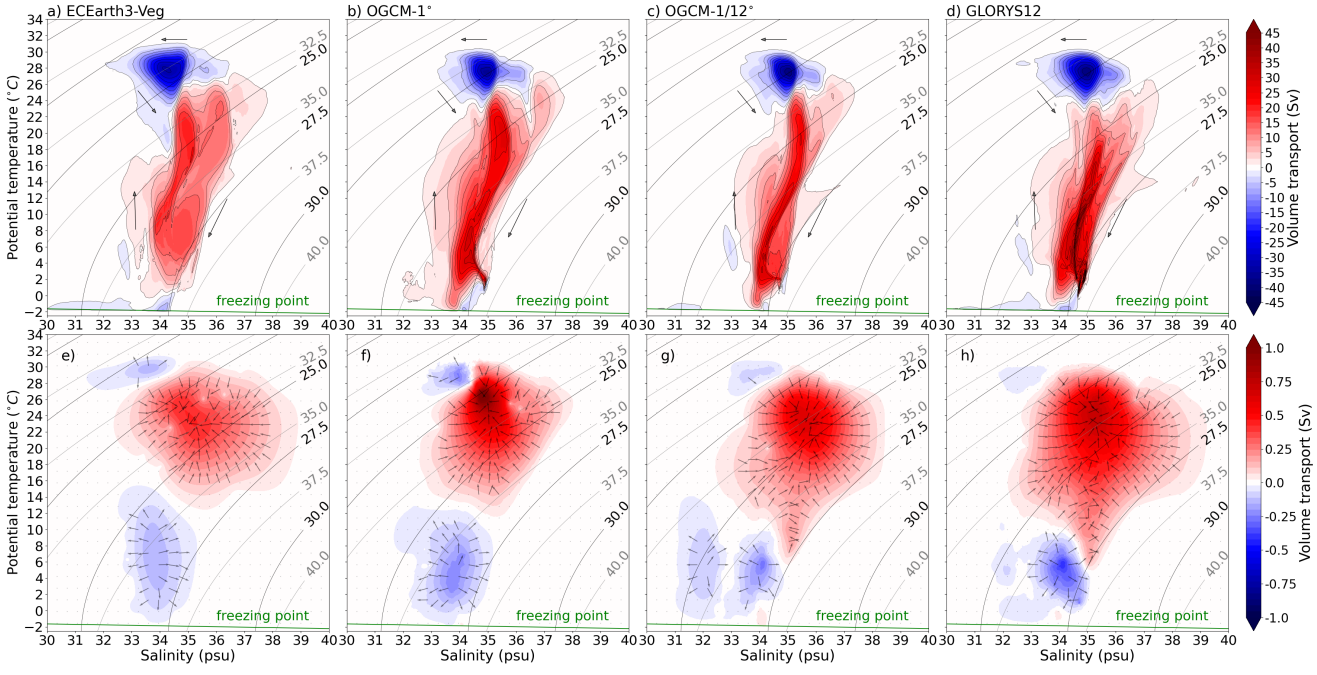

Figure 8. The diathermohaline stream function ψ (upper row) and the tendency potential χ (lower row) for EC-Earth3-Veg (first column), OGCM-1° (second column), OGCM-1/12° (third column), GLORYS12 (last column). Black (grey) contour lines show the σ_0 (σ_2) isopycnals $\left(\mathrm{kg\,m^{-3}}\right)$.

We identify also differences in the Conveyor Belt cell and the Tropical cell among the data sets. A pronounced feature is the alignment of the two cells. They are positioned at the same salinity ranges in the OGCM and GLORYS12 data while they are slightly tilted in the EC-Earth3-Veg simulation, likely since the OGCM and GLORYS12 simulations are bound by atmospheric

https://doi.org/10.5194/egusphere-2026-3561
Preprint. Discussion started: 30 June 2026

reanalysis forcing at the surface while EC-Earth3-Veg is a free-running climate model. The Tropical cell is located at lower salinities in the coupled EC-Earth3-Veg simulation with the maximum absolute value of the Tropical cell at 34.2 psu compared to 35 psu in the other data sets. In the coupled climate model data set, the Tropical cell also reaches down to 18 °C while its coldest temperature range is cancelled out by the Conveyor Belt cell in the OGCM and reanalysis data. The magnitude of the Tropical cell is smallest in the EC-Earth3-Veg simulation (-33.5 Sv), slightly higher in the OGCM-1° (-35.9 Sv) and highest in the high resolution data OGCM-1/12° (-39.4 Sv) and GLORYS12 (-38.4 Sv).

The salinity range of the Conveyor Belt cell is clearly wider in the coupled EC-Earth3-Veg simulation at most potential temperatures compared to the other data sets. The magnitude of the Conveyor Belt cell is smallest in the EC-Earth3-Veg simulation (23.3 Sv) and largest in the GLORYS12 reanalysis data set (63.2 Sv). The Conveyor Belt cells of the OGCM simulations of low and high resolution have a maximum magnitude of 31.8 Sv and 30.2 Sv respectively. The shape of the Conveyor Belt cell in the OGCM-1° differs from the high resolution OGCM in the potential temperature range 2–10 °C, which we connect to the difference caused by the missing eddy induced velocities (compare Fig. 7). Distinct warm and cold subcells in the Conveyor Belt cell is pronounced in the coupled simulation and also present in the OGCM data. These two subcells were connected to the thermally direct surface and thermally indirect deep cell in temperature–depth space by Zika et al. (2013). The GLORYS12 data show, however, a different structure where the Conveyor Belt cells appears rather structured by salinity ranges.

The tendency potential of all the data have similar shapes as described in Sect.2.4 with convergence in the centre of the domain (net evaporation) and divergence at high and low temperatures (net precipitation). The smallest magnitude in the tendency potential is shown in the coupled EC-Earth3-Veg simulation with a maximum absolute value of 0.4 Sv. The OGCM model data of coarse (fine) horizontal resolution have a maximum in the tendency potential of 1.2 Sv (0.6 Sv) and GLORYS12 has the largest maximum value of 1.4 Sv.

5.2 Diathermohaline stream function of a pre-industrial simulation and climate scenarios

Figure 9 shows the coupled EC-Earth3-Veg simulations for a PI simulation and for the three different climate scenarios ssp1-2.6, ssp3-7.0 and ssp5-8.5. The difference in the Conveyor Belt cell and the Tropical cell between the PI and PD day simulation is slightly bigger compared to the difference between PD and ssp1-2.6 scenario but clearly overreached by the differences of the ssp3-7.0 and ssp5-8.5 scenarios with respect to the PD simulation.

https://doi.org/10.5194/egusphere-2026-3561
Preprint. Discussion started: 30 June 2026

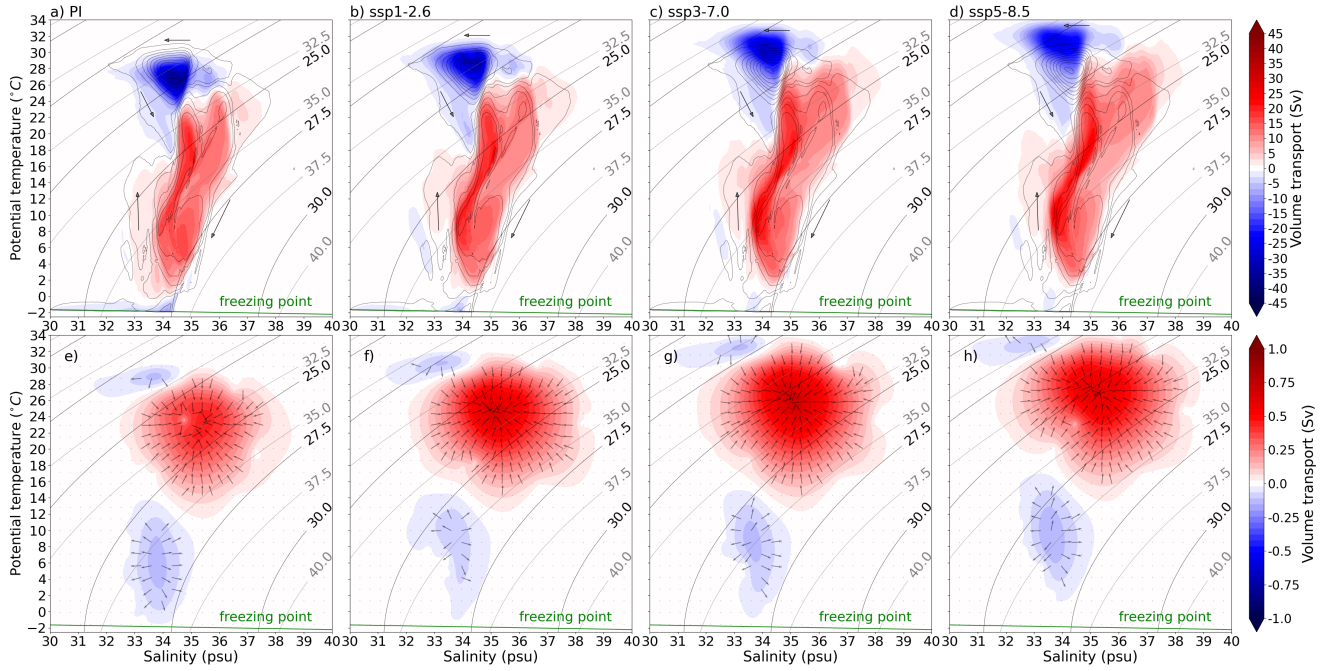

Figure 9. The diathermohaline stream function ψ (top row) and the tendency potential χ (bottom row) for EC-Earth3-Veg simulation data a) PI (1851–1860) and b)-d) climate scenarios (2091–2100). Grey contour lines in the upper row indicate the stream function from the PD (2003–2012) simulation. Isopycnals σ_0 and σ_2 are labeled in black and grey respectively $\left(\mathrm{kg\,m^{-3}}\right)$.

The WMT of both the Tropical and the Conveyor Belt cell occurs at a larger range of salinity the higher the emission scenario. While the Tropical cell is reduced in magnitude from a maximum of 36.7 Sv in the PD simulation to -26.5 Sv in the ssp5-8.5, there is no clear trend found in the maximum strength of the Conveyor Belt cell with higher emission scenarios. However, the Polar cell is reduced remarkably and shifted towards fresher water masses with stronger climate scenarios and the Cryosphere cell disappears entirely in the high emission scenario.

5.3 Heat and freshwater transport

The heat transport across isohalines and within the potential temperature range of θ to $\theta + d\theta$ is determined by $c_p \theta \left(\partial\psi/\partial\theta\right) d\theta$ (Döös et al., 2017). By integrating by parts, the heat transport of the stream function cells is defined as:

$$H\left(S\right) = -c_p \rho_0 \int_{\theta_{min}(S)}^{\theta_{max}(S)} \psi\left(S,\theta\right) d\theta, \tag{6}$$

https://doi.org/10.5194/egusphere-2026-3561
Preprint. Discussion started: 30 June 2026

and equivalent the freshwater transport as:

$$F(\theta) = -\frac{1}{S_r} \int_{S_{min}(\theta)}^{S_{max}(\theta)} \psi(S,\theta)\, dS \tag{7}$$

where we use the specific heat capacity c_p of 3992 $\mathrm{J\,kg^{-1}K^{-1}}$ and the density ρ_0 of 1026 $\mathrm{kg\,m^{-3}}$ and S_r =35 psu as reference salinity. Figure 10 shows the heat and freshwater transports of the Tropical and the Conveyor Belt cell for all analysed data sets. The heat and freshwater transports of both the OGCM Tropical cells align well with the shape of the GLORYS12 transports (panel a) and b) in Fig 10) with a larger magnitude in GLORYS12. Even if the maximum strength of the stream function cells in the OGCM-1/12° and GLORYS12 are comparable, the cell of the reanalysis data is less confined in thermohaline space which leads to a larger magnitude in the transports. Following the same argument, the Tropical cell of the EC-Earth3-Veg simulation has a larger amplitude in the heat and freshwater transport due to its extension in the thermohaline space while the magnitude of the stream function cell is smaller compared to the other data sets. Due to the position of the Tropical cell in thermohaline space, the heat transport of the EC-Earth3-Veg Tropical cell is at low salinity values. In the climate scenarios, the heat transport is shifted towards smaller salinity values and the freshwater transport towards higher potential temperatures with higher emission scenarios. Since the magnitude of the Tropical cell is reduced in the scenarios, the heat and freshwater transport is decreasing (compare Sect. 5.2).

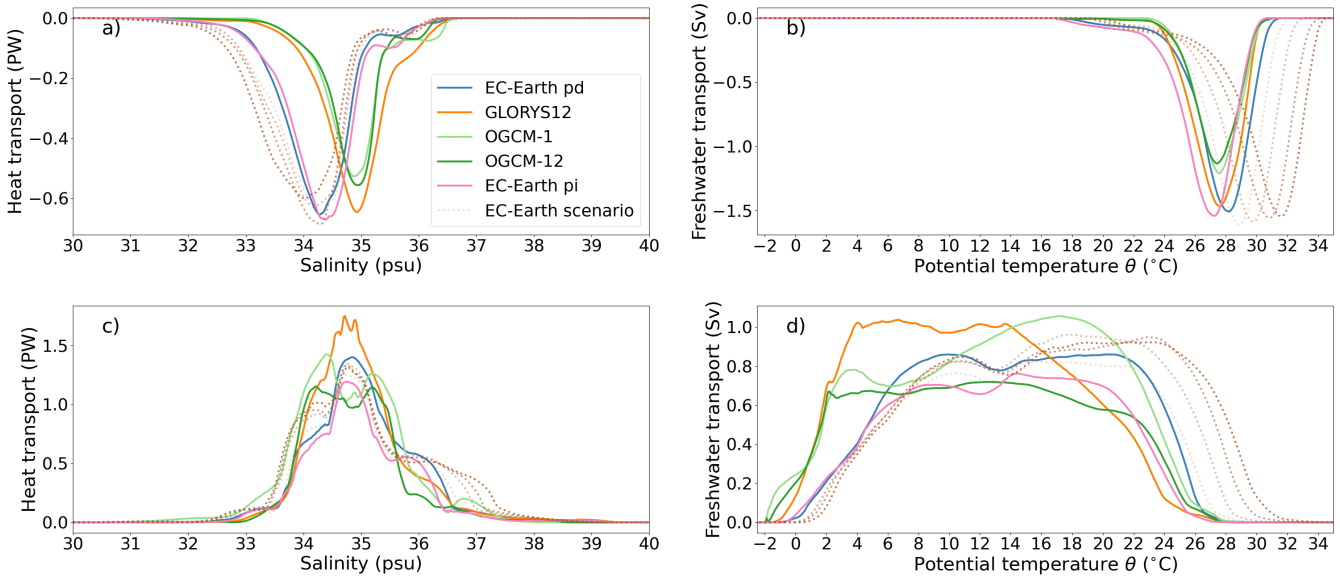

Figure 10. Heat (left) and freshwater (right) transport of the Tropical cell (upper row) and the Conveyor Belt cell (lower row) for the four data sets described in table 1. Dotted lines indicate the different scenarios with darker colours for higher scenario numbers.

The Conveyor Belt cell of the GLORYS12 data and the EC-Earth3-Veg simulation has the maximum heat transport at salinities where the heat transports of both OGCM model data have the local minima of its dipole structure (panel c) of Fig.

https://doi.org/10.5194/egusphere-2026-3561
Preprint. Discussion started: 30 June 2026

10). The EC-Earth3-Veg Conveyor Belt cell shows less heat transport at low salinities due to the overlap with the Tropical cell at high temperatures but more heat transport at higher salinities but due to the large salinities range. This extension of the EC-Earth3-Veg Conveyor belt cell induces also a freshwater transport that is comparable to the other data sets despite the smaller magnitude of the stream function cell in the EC-Earth3-Veg simulation. In the OGCM simulations, the low resolution case shows a larger heat transport which we connect to the missing counter parts from the eddy induced velocities. The Conveyor Belt cell of the OGCM-1/12° is characterized by the smallest salinity range resulting in a overall small freshwater transport compared to the other data sets. In the climate scenarios, the Conveyor Belt cell is widening in the salinity range which can be seen in the heat transport, specifically in the high salinity values. This leads as well to a larger freshwater transport with higher emission scenarios which is shifted towards higher temperatures.

6 Discussion under the use of ocean basins water volume distributions

In the previous section, we compared the diathermohaline stream function computed for data sets of multiple horizontal resolutions of a coupled climate model, ocean hindcast simulations forced by reanalysis data and ocean reanalysis data. Here we summarize the main differences by comparing the results to the volume distributions of each ocean basin that is defined as

$$v(S,\theta) = \frac{1}{t_1 - t_0} \int_{t_0}^{t_1} \frac{\partial^2 V}{\partial S \partial \theta} dt \tag{8}$$

where $V = V(S,\theta,t)$ is the volume with a salinity less than S and a temperature less then θ (Hieronymus et al., 2014).

https://doi.org/10.5194/egusphere-2026-3561
Preprint. Discussion started: 30 June 2026

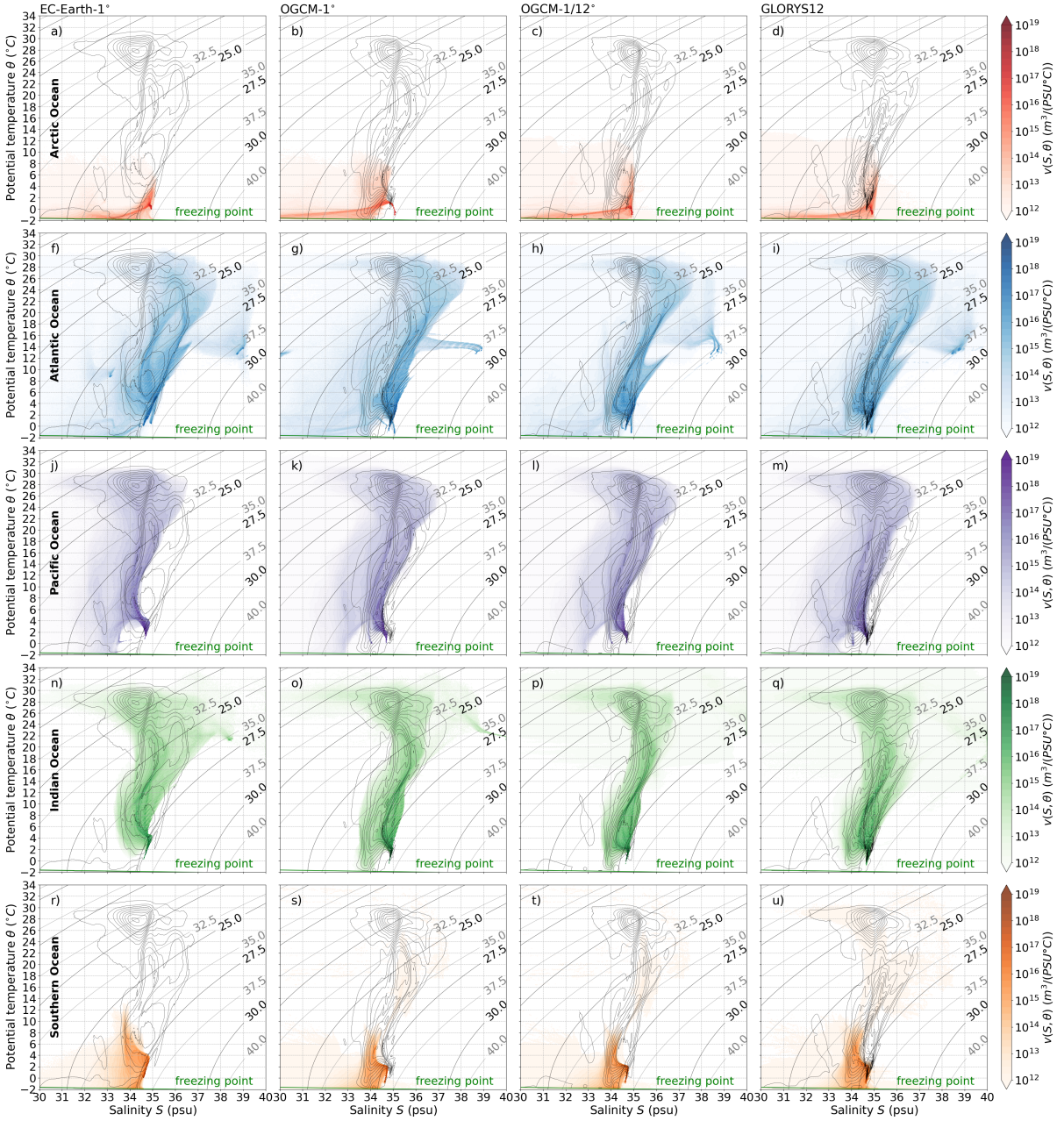

Figure 11. Volume distribution function $v(S,\theta)$ of the ocean's basins water for the four data sets described in table 1. The red water volume distribution in the first row is the Arctic water, blue in the second row the Atlantic, purple in the third row the Pacific, green in the fourth row the Indian and orange in the last row represents water around Antarctica. The latitude defining the boundary for the Southern Ocean is indicated as vertical dashed line in Fig. 4. The grey contour lines are the diathermohaline stream function. Isopycnals σ_0 and σ_2 are labelled in black and grey respectively $\left(\mathrm{kg\,m^{-3}}\right)$.

https://doi.org/10.5194/egusphere-2026-3561
Preprint. Discussion started: 30 June 2026

The Tropical cell is weaker in the low resolution models, of both the coupled and ocean hindcast, which suggests an under representation of the WMT in the subtropical gyres or an stronger cancelling effect by the Conveyor Belt cell compared to the high-resolution data. The stream function of the EC-Earth3-Veg (OGCM-1°) is computed from the mass transports (Eulerian mean velocities). Since the validation data set does not show much contribution from the eddy induced velocities in the range of the Tropical cell, we speculate that the different strengths in the Tropical cell is not caused by the missing subgrid parametrization of the advective scheme. The Tropical cell stretches towards lower temperatures and is located at lower salinities in the EC-Earth3-Veg simulation which has a positive precipitation bias in the subtropics of the Southern Hemisphere (Döscher et al., 2022). Accordingly, the water volume distribution in Fig. 11 stretches out to lower salinities above 20 °C in the Pacific and the Indian ocean basins of the EC-Earth3-Veg simulation.

A major difference of the Conveyor Belt cells is a wider salinity range in the EC-Earth3-Veg data. The cell of this data set also shows a stronger heat transport at salinities between 36–36.5 psu which we connect to water masses between 10–15 °C that are mainly water masses in the Atlantic Ocean. In the EC-Earth3-Veg simulation, however, the Indian Ocean shows a larger amount if water volume saltier than 36 psu for potential temperatures warmer than 20 °C. This is presumably contributing as well to a wider salinity range of the Conveyor Belt cell in the EC-Earth3-Veg simulation.

The Pacific as well as the Indian Ocean water warmer than 5 °C appears to reach lower salinities in EC-Earth3-Veg data compared to the other data sets (Fig. 11). This, however, does not lead to a stronger heat transport in the low salinities because the Conveyor Belt cell of the other data sets are spanning a wider temperature range due to the cancellation effects by the Tropical and Polar cells in the EC-Earth3-Veg simulation. Döös et al. (2012) also notes that a faster ocean lead to a smaller salinity range and a slower ocean has a wider salinity range in the diathermohaline stream function.

The Polar cell is most pronounced in the EC-Earth3-Veg simulation while this data set has also the weakest bottom cell in the meridional overturning stream functions as function of depth. The warm bias in the Southern Ocean in the EC-Earth3-Veg model (Döscher et al., 2022) could result in the salinitfication branch of the Conveyor Belt cell at warmer temperatures and, thus, to a clearer separation of the Polar Cell and the Conveyor Belt cell. This leads to a stronger Polar cell even if the bottom water in the overturning stream function appears to be weaker. Additional, the coldest water in the Indian ocean is warmer at around 34 psu with a minimum temperature of about 1 °C while the other data sets contain more water volume close to the freezing line in the Indian Ocean. Furthermore, the spin-up time in the EC-Earth3-Veg simulation is longer and which could lead to a more pronounced Polar cell since this cell is specifically sensitive to model drift (Döös et al., 2012).

In the climate scenarios, the Tropical cell is located at lower salinities with higher emission scenarios indicating a freshening of the subtropical gyres (Sathyanarayanan et al., 2021). The Tropical cell and the Conveyor Belt cell is shifted towards higher temperatures whereby the difference is larger the warmer the temperatures. This is expected since this is mainly surface near water that respond quicker to climate change and the propagation of the heat uptake to the ocean interior occurs on slower time spans (Marshall and Zanna, 2014). The widening of Conveyor Belt cell in the salinity range of the climate scenarios might be connected to an accelerated hydrological cycle.

https://doi.org/10.5194/egusphere-2026-3561
Preprint. Discussion started: 30 June 2026

7 Conclusions

We developed a modular code to compute the diathermohaline stream function that is easy to adapt for other data sets. Analysing the sensitivity of the stream function on different model output variables shows that the impact of fluctuation terms on a monthly time scale is negligible when computing the volume transports from time averaged velocities and time averaged layer thicknesses. The eddy induced velocities, however, contribute significantly to the stream function. Furthermore, we show that the tendency potential can be mainly connected to net sinks and sources of freshwater mainly due to evaporation and precipitation. Using the diathermohaline stream function makes it possible to identify quickly the differences in the global WMT in various data sets by combining three-dimensional ocean dynamics variables and two variables of the global thermohaline state in only two figures. It is therefore a powerful tool that contains a large amount of information about the WMT on a time averaged and global scale. Thus, it is a method that offers a beneficial potential for model comparison projects and model development processes. By using different example data we highlight how the framework can contribute to those comparison projects of gridded ocean data. In combination with ocean volume distribution functions indications to the geographical locations are given. And yet, it cannot explain whether the differences occurring due to the dynamical or the thermohaline fields nor can it identify precisely the geographical regions where the differences are largest. It needs further investigations to reveal the processes that are represented differently in the data sets. More detailed analysis about the geographical location can be applied by remapping layers of the stream function into geographical space as described in Döös et al. (2012).

https://doi.org/10.5194/egusphere-2026-3561
Preprint. Discussion started: 30 June 2026

Appendix A: Sensitivity of the stream function with resolution of the thermohaline space

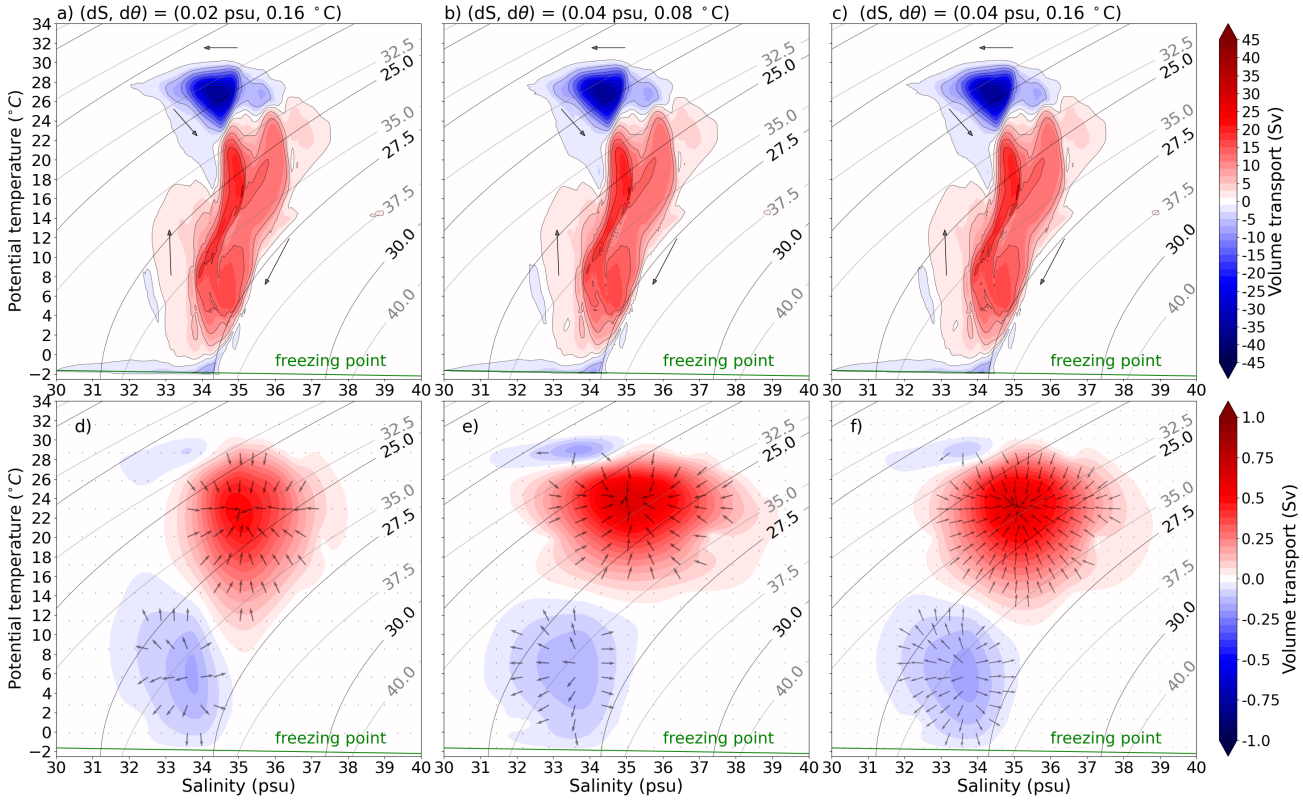

Figure A1. Sensitivity of the stream function ψ and the tendency potential χ to the resolution of the tracer space with decreased resolution in a) potential temperature, b) in salinity and c) both temperature and salinity. Isopycnals σ_0 and σ_2 are labelled in black and grey respectively $\left(\mathrm{kg\,m^{-3}}\right)$.

https://doi.org/10.5194/egusphere-2026-3561
Preprint. Discussion started: 30 June 2026

Code and data availability. The ocean data of the EC-Earth3-Veg validation simulation are archived on the Bolin Center data base https://doi.org/10.17043/jung-2026-ec-earth3-veg-1 (Jung, 2026). The satellite data SMOS-SMAP are taken from https://doi.org/10.48670/mds-00369 (SSS SMOS/SMAP L4 OI - LOPS-v2023). CMIP6 data of EC-Earth3-Veg simulations are accessible with https://doi.org/10.22033/ESGF/CMIP6.642 (EC-Earth Consortium). The GLORYS12 data are available as regular gridded interpolated data on the Copernicus data base https://doi.org/10.48670/moi-00021 (Global Ocean Physics Reanalysis) and on the native Arakawa-C grid in the mercator data catalogue http://tds.mercator-ocean.fr/thredds/catalog.html (Mercator Ocean International). The OGCM-1° are provided on the NOC supercomputer Jasmin https://www.jasmin.ac.uk/users/access/ (JASMIN facility; Lawrence et al., 2013) and the OGCM-1/12° data are made publicly available by NERC https://gws-access.jasmin.ac.uk/public/nemo/ (NOC Marine System Modelling group). We provide the tendencies for all investigated data sets, together with the code for the diathermohaline stream function on Zenodo https://doi.org/10.5281/zenodo.20724367 (Jung et al., 2026).

Author contributions. The conceptualisation of the present work was done by K. Döös and V. Jung. The implementation of the diathermohaline stream function was developed by V. Jung, J. Kjellsson, A. Campino and K. Döös. V. Jung analysed the model and satellite data and wrote the manuscript. All authors contributed to discussing the results and reviewing the manuscript.

Competing interests. The authors declare that they have no conflict of interest.

Acknowledgements. This work is supported by the Swedish National Space Agency Rymdstyrelsen, Grant Agreement No. 2022-00141 The computations and data handling were enabled by resources provided by the National Academic Infrastructure for Supercomputing in Sweden (NAISS) at the National Supercomputer Centre (NSC) partially funded by the Swedish Research Council through grant agreement no. 2022-06725. Further, this work used JASMIN, the UK's collaborative data analysis environment and contains data supplied by the Natural Environment Research Council (NERC) and provided by the National Oceanography Centre Southampton (NOC) (Lawrence et al., 2013). Results are further generated with MERCATOR OCEAN products and data were provided by the Swedish Meteorological and Hydrological Institute (SMHI). This study has been conducted using E.U. Copernicus Marine Service Information.

https://doi.org/10.5194/egusphere-2026-3561
Preprint. Discussion started: 30 June 2026

References

Bacon, S., Aksenov, Y., Fawcett, S., and Madec, G.: Arctic mass, freshwater and heat fluxes: methods and modelled seasonal variability, Philosophical Transactions of the Royal Society A: Mathematical, Physical and Engineering Sciences, 373, 20140 169, https://doi.org/10.1098/rsta.2014.0169, 2015.

Ballarotta, M., Falahat, S., Brodeau, L., and Döös, K.: On the glacial and interglacial thermohaline circulation and the associated transports of heat and freshwater, Ocean Science, 10, 907–921, https://doi.org/10.5194/os-10-907-2014, 2014.

Berglund, S., Döös, K., and Nycander, J.: Lagrangian tracing of the water–mass transformations in the Atlantic Ocean, Tellus A: Dynamic Meteorology and Oceanography, 69, https://doi.org/10.1080/16000870.2017.1306311, 2017.

Berglund, S., Döös, K., Campino, A. A., and Nycander, J.: The Water Mass Transformation in the Upper Limb of the Overturning Circulation in the Southern Hemisphere, Journal of Geophysical Research: Oceans, 126, e2021JC017 330, https://doi.org/10.1029/2021JC017330, 2021.

Dai, A., Qian, T., Trenberth, K. E., and Milliman, J. D.: Changes in Continental Freshwater Discharge from 1948 to 2004, Journal of Climate, 22, 2773–2792, https://doi.org/10.1175/2008JCLI2592.1, 2009.

Drake, H. F., Bailey, S., Dussin, R., Griffies, S. M., Krasting, J., MacGilchrist, G., Stanley, G., Tesdal, J.-E., and Zika, J. D.: Water Mass Transformation Budgets in Finite-Volume Generalized Vertical Coordinate Ocean Models, Journal of Advances in Modeling Earth Systems, 17, e2024MS004 383, https://doi.org/10.1029/2024MS004383, 2025.

Dussin, R., Barnier, B., Brodeau, L., and Molines, J. M.: The making of the Drakkar forcing set DFS5, DRAKKAR/MyOcean Rep, 104, 16, https://doi.org/10.5281/zenodo.1209242, 2016.

Döscher, R., Acosta, M., Alessandri, A., Anthoni, P., Arsouze, T., Bergman, T., Bernardello, R., Boussetta, S., Caron, L.-P., Carver, G., Castrillo, M., Catalano, F., Cvijanovic, I., Davini, P., Dekker, E., Doblas-Reyes, F. J., Docquier, D., Echevarria, P., Fladrich, U., Fuentes-Franco, R., Gröger, M., v. Hardenberg, J., Hieronymus, J., Karami, M. P., Keskinen, J.-P., Koenigk, T., Makkonen, R., Massonnet, F., Ménégoz, M., Miller, P. A., Moreno-Chamarro, E., Nieradzik, L., van Noije, T., Nolan, P., O'Donnell, D., Ollinaho, P., van den Oord, G., Ortega, P., Prims, O. T., Ramos, A., Reerink, T., Rousset, C., Ruprich-Robert, Y., Le Sager, P., Schmith, T., Schrödner, R., Serva, F., Sicardi, V., Sloth Madsen, M., Smith, B., Tian, T., Tourigny, E., Uotila, P., Vancoppenolle, M., Wang, S., Wårlind, D., Willén, U., Wyser, K., Yang, S., Yepes-Arbós, X., and Zhang, Q.: The EC-Earth3 Earth system model for the Coupled Model Intercomparison Project 6, Geoscientific Model Development, 15, 2973–3020, https://doi.org/10.5194/gmd-15-2973-2022, 2022.

Döös, K. and Webb, D. J.: The Deacon Cell and the Other Meridional Cells of the Southern Ocean, Journal of Physical Oceanography, 24, 429–442, https://doi.org/10.1175/1520-0485(1994)024<0429:TDCATO>2.0.CO;2, 1994.

Döös, K., Nilsson, J., Nycander, J., Brodeau, L., and Ballarotta, M.: The World Ocean Thermohaline Circulation, Journal of Physical Oceanography, 42, 1445–1460, https://doi.org/10.1175/JPO-D-11-0163.1, 2012.

Döös, K., Kjellsson, J., Zika, J., Laliberté, F., Brodeau, L., and Campino, A. A.: The Coupled Ocean–Atmosphere Hydrothermohaline Circulation, Journal of Climate, 30, 631–647, https://doi.org/10.1175/JCLI-D-15-0759.1, 2017.

Döös, K., Lundberg, P., and Campino, A. A.: Basic Numerical Methods in Meteorology and Oceanography, Stockholm University Press, https://doi.org/10.16993/bbs, 2022.

EC-Earth Consortium: EC-Earth3-Veg model output prepared for CMIP6. Earth System Grid Federation [data set], https://doi.org/https://doi.org/10.22033/ESGF/CMIP6.642, 2019.

https://doi.org/10.5194/egusphere-2026-3561
Preprint. Discussion started: 30 June 2026

Evans, D. G., Zika, J. D., Naveira Garabato, A. C., and Nurser, A. J. G.: The imprint of Southern Ocean overturning on seasonal water mass variability in Drake Passage, Journal of Geophysical Research: Oceans, 119, 7987–8010, https://doi.org/10.1002/2014JC010097, 2014.

Evans, D. G., Toole, J., Forget, G., Zika, J. D., Garabato, A. C. N., Nurser, A. J. G., and Yu, L.: Recent Wind-Driven Variability in Atlantic Water Mass Distribution and Meridional Overturning Circulation, Journal of Physical Oceanography, 47, 633–647, https://doi.org/10.1175/JPO-D-16-0089.1, 2017.

Evans, D. G., Zika, J. D., Naveira Garabato, A. C., and Nurser, A. J. G.: The Cold Transit of Southern Ocean Upwelling, Geophysical Research Letters, 45, 13,386–13,395, https://doi.org/10.1029/2018GL079986, 2018.

Gent, P. R. and Mcwilliams, J. C.: Isopycnal Mixing in Ocean Circulation Models, Journal of Physical Oceanography, 20, 150–155, https://doi.org/10.1175/1520-0485(1990)020<0150:IMIOCM>2.0.CO;2, 1990.

Global Ocean Physics Reanalysis: E.U. Copernicus Marine Service Information (CMEMS). Marine Data Store (MDS) [data set], https://doi.org/10.48670/moi-00021, creation 2012.

Groeskamp, S., Zika, J. D., McDougall, T. J., Sloyan, B. M., and Laliberté, F.: The Representation of Ocean Circulation and Variability in Thermodynamic Coordinates, Journal of Physical Oceanography, 44, 1735–1750, https://doi.org/10.1175/JPO-D-13-0213.1, 2014.

Groeskamp, S., Griffies, S. M., Iudicone, D., Marsh, R., Nurser, A. J. G., and Zika, J. D.: The Water Mass Transformation Framework for Ocean Physics and Biogeochemistry, Annual Review of Marine Science, 11, 271–305, https://doi.org/10.1146/annurev-marine-010318-095421, 2019.

Hieronymus, M., Nilsson, J., and Nycander, J.: Water Mass Transformation in Salinity–Temperature Space, Journal of Physical Oceanography, 44, 2547–2568, https://doi.org/10.1175/JPO-D-13-0257.1, 2014.

Holmes, R. M., Zika, J. D., and England, M. H.: Diathermal Heat Transport in a Global Ocean Model, Journal of Physical Oceanography, 49, 141–161, https://doi.org/10.1175/JPO-D-18-0098.1, 2019.

Isachsen, P. E., Mauritzen, C., and Svendsen, H.: Dense water formation in the Nordic Seas diagnosed from sea surface buoyancy fluxes, Deep Sea Research Part I: Oceanographic Research Papers, 54, 22–41, https://doi.org/10.1016/j.dsr.2006.09.008, 2007.

Iudicone, D., Madec, G., and McDougall, T. J.: Water-Mass Transformations in a Neutral Density Framework and the Key Role of Light Penetration, Journal of Physical Oceanography, 38, 1357–1376, https://doi.org/10.1175/2007JPO3464.1, 2008.

JASMIN facility: https://www.jasmin.ac.uk/users/access/, (last access: 27 June 2026).

Jean-Michel, L., Eric, G., Romain, B.-B., Gilles, G., Angélique, M., Marie, D., Clément, B., Mathieu, H., Olivier, L. G., Charly, R., Tony, C., Charles-Emmanuel, T., Florent, G., Giovanni, R., Mounir, B., Yann, D., and Pierre-Yves, L. T.: The Copernicus Global 1/12° Oceanic and Sea Ice GLORYS12 Reanalysis, Frontiers in Earth Science, 9, https://doi.org/10.3389/feart.2021.698876, 2021.

Jung, V.: Pre-industrial global ocean data from an EC-Earth3-Veg climate simulation for 1850-1860, Bolin Center Database [data set], 2026.

Jung, V., Aldama-Campino, A., Kjellsson, J., and Döös, K.: The diathermohaline stream function method (v2026.1), Zenodo [code and data set], 2026.

Kjellsson, J.: Weakening of the global atmospheric circulation with global warming, Climate Dynamics, 45, 975–988, https://doi.org/10.1007/s00382-014-2337-8, 2015.

Kjellsson, J., Döös, K., Laliberté, F. B., and Zika, J. D.: The Atmospheric General Circulation in Thermodynamical Coordinates, Journal of the Atmospheric Sciences, 71, 916–928, https://doi.org/10.1175/JAS-D-13-0173.1, 2014.

Kolodziejczyk, N., Hamon, M., Boutin, J., Vergely, J.-L., Reverdin, G., Supply, A., and Reul, N.: Objective Analysis of SMOS and SMAP Sea Surface Salinity to Reduce Large-Scale and Time-Dependent Biases from Low to High Latitudes, Journal of Atmospheric and Oceanic Technology, 38, 405–421, https://doi.org/10.1175/JTECH-D-20-0093.1, 2021.

https://doi.org/10.5194/egusphere-2026-3561
Preprint. Discussion started: 30 June 2026

Lawrence, B. N., Bennett, V. L., Churchill, J., Juckes, M., Kershaw, P., Pascoe, S., Pepler, S., Pritchard, M., and Stephens, A.: Storing and manipulating environmental big data with JASMIN, in: 2013 IEEE International Conference on Big Data, pp. 68–75, https://doi.org/10.1109/BigData.2013.6691556, 2013.

Li, Z., Chao, Y., and McWilliams, J. C.: Computation of the Streamfunction and Velocity Potential for Limited and Irregular Domains, Monthly Weather Review, 134, 3384–3394, https://doi.org/10.1175/MWR3249.1, 2006.

Madec, G. and Imbard, M.: A global ocean mesh to overcome the North Pole singularity, Climate Dynamics, 12, 381–388, https://doi.org/10.1007/BF00211684, 1996.

Madec, G., Bourdallé-Badie, R., Bouttier, P.-A., Bricaud, C., Bruciaferri, D., Calvert, D., Chanut, J., Clementi, E., Coward, A., Delrosso, D., Ethé, C., Flavoni, S., Graham, T., Harle, J., Iovino, D., Lea, D., Lévy, C., Lovato, T., Martin, N., Masson, S., Mocavero, S., Paul, J., Rousset, C., Storkey, D., Storto, A., and Vancoppenolle, M.: NEMO ocean engine, https://doi.org/10.5281/zenodo.3248739, 2017.

Marshall, D. P. and Zanna, L.: A Conceptual Model of Ocean Heat Uptake under Climate Change, Journal of Climate, 27, 8444–8465, https://doi.org/10.1175/JCLI-D-13-00344.1, 2014.

Marshall, J. and Speer, K.: Closure of the meridional overturning circulation through Southern Ocean upwelling, Nature Geoscience, 5, 171–180, https://doi.org/10.1038/ngeo1391, 2012.

Marshall, J., Jamous, D., and Nilsson, J.: Reconciling thermodynamic and dynamic methods of computation of water-mass transformation rates, Deep Sea Research Part I: Oceanographic Research Papers, 46, 545–572, https://doi.org/10.1016/S0967-0637(98)00082-X, 1999.

Mercator Ocean International: Data catalogue [data set], http://tds.mercator-ocean.fr/thredds/catalog.html, downloaded 2024.

NOC Marine System Modelling group: https://gws-access.jasmin.ac.uk/public/nemo/ [data set] (last access: 27 June 2026).

Nurser, A. J. G., Marsh, R., and Williams, R. G.: Diagnosing Water Mass Formation from Air–Sea Fluxes and Surface Mixing, Journal of Physical Oceanography, 29, 1468–1487, https://doi.org/10.1175/1520-0485(1999)029<1468:DWMFFA>2.0.CO;2, 1999.

Nycander, J., Nilsson, J., Döös, K., and Broström, G.: Thermodynamic Analysis of Ocean Circulation, Journal of Physical Oceanography, 37, 2038–2052, https://doi.org/10.1175/JPO3113.1, 2007.

O'Neill, B. C., Tebaldi, C., van Vuuren, D. P., Eyring, V., Friedlingstein, P., Hurtt, G., Knutti, R., Kriegler, E., Lamarque, J.-F., Lowe, J., Meehl, G. A., Moss, R., Riahi, K., and Sanderson, B. M.: The Scenario Model Intercomparison Project (ScenarioMIP) for CMIP6, Geoscientific Model Development, 9, 3461–3482, https://doi.org/10.5194/gmd-9-3461-2016, 2016.

Pemberton, P., Nilsson, J., Hieronymus, M., and Meier, H. E. M.: Arctic Ocean Water Mass Transformation in S–T Coordinates, Journal of Physical Oceanography, 45, 1025–1050, https://doi.org/10.1175/JPO-D-14-0197.1, 2015.

Roberts, M. J., Jackson, L. C., Roberts, C. D., Meccia, V., Docquier, D., Koenigk, T., Ortega, P., Moreno-Chamarro, E., Bellucci, A., Coward, A., Drijfhout, S., Exarchou, E., Gutjahr, O., Hewitt, H., Iovino, D., Lohmann, K., Putrasahan, D., Schiemann, R., Seddon, J., Terray, L., Xu, X., Zhang, Q., Chang, P., Yeager, S. G., Castruccio, F. S., Zhang, S., and Wu, L.: Sensitivity of the Atlantic Meridional Overturning Circulation to Model Resolution in CMIP6 HighResMIP Simulations and Implications for Future Changes, Journal of Advances in Modeling Earth Systems, 12, e2019MS002 014, https://doi.org/10.1029/2019MS002014, 2020.

Sathyanarayanan, A., Köhl, A., and Stammer, D.: Ocean Salinity Changes in the Global Ocean under Global Warming Conditions. Part I: Mechanisms in a Strong Warming Scenario, Journal of Climate, 34, 8219–8236, https://doi.org/10.1175/JCLI-D-20-0865.1, 2021.

Shukla, J. and Saha, K. R.: Computation of Non-Divergent Streamfunction and Irrotational Velocity Potential from the Observed Winds, Monthly Weather Review, 102, 419–425, https://doi.org/10.1175/1520-0493(1974)102<0419:CONDSA>2.0.CO;2, 1974.

Sieker, T., Kjellsson, J., and Park, W.: Impact of ocean resolution on the North Atlantic bias in the FOCI-OpenIFS climate model, Climate Dynamics, 64, 144, https://doi.org/10.1007/s00382-026-08110-6, 2026.

https://doi.org/10.5194/egusphere-2026-3561
Preprint. Discussion started: 30 June 2026

Skliris, N., Zika, J. D., Nurser, G., Josey, S. A., and Marsh, R.: Global water cycle amplifying at less than the Clausius-Clapeyron rate, Scientific Reports, 6, 38 752, https://doi.org/10.1038/srep38752, 2016.

Skliris, N., Zika, J. D., Herold, L., Josey, S. A., and Marsh, R.: Mediterranean sea water budget long-term trend inferred from salinity observations, Climate Dynamics, 51, 2857–2876, https://doi.org/10.1007/s00382-017-4053-7, 2018.

Speer, K. G.: A note on average cross-isopycnal mixing in the North Atlantic ocean, Deep Sea Research Part I: Oceanographic Research Papers, 44, 1981–1990, https://doi.org/10.1016/S0967-0637(97)00054-X, 1997.

SSS SMOS/SMAP L4 OI - LOPS-v2023: E.U. Copernicus Marine Service Information (CMEMS). Marine Data Store (MDS) [data set], https://doi.org/10.48670/mds-00369, downloaded 2025.

Stewart, A. L.: Mesoscale, Tidal, and Seasonal/Interannual Drivers of the Weddell Sea Overturning Circulation, Journal of Physical Oceanography, 51, 3695–3722, https://doi.org/10.1175/JPO-D-20-0320.1, 2021.

Treguier, A. M., Held, I. M., and Larichev, V. D.: Parameterization of Quasigeostrophic Eddies in Primitive Equation Ocean Models, Journal of Physical Oceanography, 27, 567–580, https://doi.org/10.1175/1520-0485(1997)027<0567:POQEIP>2.0.CO;2, 1997.

Walin, G.: A theoretical framework for the description of estuaries, Tellus, 29, 128–136, https://doi.org/10.3402/tellusa.v29i2.11337, 1977.

Walin, G.: On the relation between sea-surface heat flow and thermal circulation in the ocean, Tellus A: Dynamic Meteorology and Oceanography, 34, https://doi.org/10.3402/tellusa.v34i2.10801, 1982.

Watterson, I. G.: Decomposition of Global Ocean Currents Using a Simple Iterative Method, Journal of Atmospheric and Oceanic Technology, 18, 691–703, https://doi.org/10.1175/1520-0426(2001)018<0691:DOGOCU>2.0.CO;2, 2001.

Wilson, C., Aksenov, Y., Rynders, S., Kelly, S. J., Krumpen, T., and Coward, A. C.: Significant variability of structure and predictability of Arctic Ocean surface pathways affects basin-wide connectivity, Communications Earth & Environment, 2, 164, https://doi.org/10.1038/s43247-021-00237-0, 2021.

Zika, J. D., England, M. H., and Sijp, W. P.: The Ocean Circulation in Thermohaline Coordinates, Journal of Physical Oceanography, 42, 708–724, https://doi.org/10.1175/JPO-D-11-0139.1, 2012.

Zika, J. D., Sijp, W. P., and England, M. H.: Vertical Heat Transport by Ocean Circulation and the Role of Mechanical and Haline Forcing, Journal of Physical Oceanography, 43, 2095–2112, https://doi.org/10.1175/JPO-D-12-0179.1, 2013.

Zika, J. D., Skliris, N., Nurser, A. J. G., Josey, S. A., Mudryk, L., Laliberté, F., and Marsh, R.: Maintenance and Broadening of the Ocean's Salinity Distribution by the Water Cycle, Journal of Climate, 28, 9550–9560, https://doi.org/10.1175/JCLI-D-15-0273.1, 2015.